Chapter 4

NON-LINEAR RESPONSE OF THE TOTAL ELECTRON-YIELD SIGNAL TO THE X-RAY ABSORPTION COEFFICIENT

4.1. Is 'Near-Surface Disorder' the Origin of Reduced X-ray Absorption Fine Structure Amplitudes Detected by Total Electron-Yield Techniques?

4.1.1. Introduction

Considerable uncertainty about the accuracy of X-ray absorption fine structure (XAFS) information determined by total electron-yield (TEY) measurements has persisted since unrealistically low extended X-ray absorption fine-structure (EXAFS) amplitudes have been noticed in several studies (e.g. in [1-7]). Reliable EXAFS amplitudes are a prerequisite for the determination of meaningful coordination numbers, and their accuracy is especially desirable for angle-dependent studies of non-cubic materials [8]. Perhaps with the exception of measurements on thin foil samples [2,4], the origin of the distorted amplitude information has remained unclear [4,5,7,9]. At least one group of authors [1,3] appears to have adopted the hypothesis first put forward by Erbil *et al*. [4], which states that the EXAFS amplitude might be reduced because the TEY signal is sensitive to structural disorder in the near-surface region of the sample. Taken *prima facie*, this argument may seem plausible since the TEY signal originates in an ultrathin surface region, and the presence of a damaged layer and/or lattice disruptions due to, e.g., (sub)oxide formation could indeed modify the fine-structure amplitudes. However, many of the reported anomalous TEY amplitudes hardly fit the pattern expected for a truly disordered sample. The EXAFS analysis of structurally disordered samples does normally reveal large Debye-Waller factors, and often also deviations from the harmonic limit (characterised by Gaussian pair distributions) in which the Debye-Waller description of the amplitude attenuation is valid [10]. Fourier-transformed spectra of highly disordered samples should also exhibit reduced pair correlations, especially for higher coordination shells. Contrary to these expectations, it has repeatedly been shown that the anomalous EXAFS amplitudes obtained from TEY measurements are uniformly reduced by an almost *constant* factor, and XAFS contributions from higher coordination shells have always been visible [1,3-5].

The results of an *in situ* TEY EXAFS investigation of the annealing behaviour of metallic nickel under hydrogen add evidence that 'near-surface disorder' is unlikely to be the main origin of the reduced TEY EXAFS amplitudes.

4.1.2. Experimental

Experiments were carried out at Daresbury Laboratory with the electron storage ring operating at a beam current of 200 ± 50 mA. Measurements were performed at beamline 8.1 using a double crystal Si(220) monochromator with a resolution of approximately 1.5 eV at the Ni K-edge [11]. The beam was focused by a Pt-coated toroidal mirror, resulting in a v-shaped beamspot at the sample which did not exceed a diameter of 3 mm in any direction. The incident X-ray flux was monitored by an ion chamber filled with an Ar/He mixture exhibiting 20% absorption at the Ni K-edge. Rejection of higher beam harmonics was achieved by keeping the monochromator crystal gratings detuned at 50% of maximum reflectivity [12]. A transmission spectrum of a Ni foil (thickness: 8 μm, 99.99% pure, Goodfellow U.K.) was obtained by monitoring the transmitted beam intensity with a second ion chamber filled with an Ar/He mixture exhibiting 80% absorbance at the Ni K-edge.

A temper annealed, diamond-polished (final diamond grain size: 0.5 μm) polycrystalline Ni wafer (60 mm × 14 mm × 1 mm, 99.99% pure, Goodfellow U.K.) was mounted in the leak-tested TEY cell described in section 2.4. The TEY current was recorded using two Keithley preamplifiers, one connected to the sample and the other to the biased (+104 V) collector plate. No difference between the collector and sample currents was detected, except for a small, constant positive offset of the collector current due to the formation of spurious charges in the beam path and by scattered X-rays. The angle of X-ray incidence during the TEY measurements was constant at $5° \pm 1°$ with respect to the sample surface. Pure hydrogen (BOC, 99.99%) was used for reductive heat treatments and as the TEY detector gas (flow rate approximately 20 ml per minute). The X-ray absorption spectrum of the Ni wafer was first measured at room temperature in its freshly polished state. After 3 hours annealing in hydrogen at 400°C and slow cooling (temperature gradient between 5°C and 10°C per minute) to room temperature the measurement was repeated. Subsequent treatment of the sample at 600°C followed the same sequence of procedures.

4.1.3. Results and Discussion

It is well established that hydrogen reduces nickel oxide quantitatively to metallic Ni at temperatures over 350°C [13]. Monolayer amounts of oxygen adsorbed on Ni have previously been shown to decompose at temperatures between approximately 100°C and 350°C [14], and annealing at temperatures as low as 400°C is a standard method for obtaining order in single-crystalline Ni samples [15]. The annealing conditions employed in this study are therefore expected to decompose oxidic near-surface species and to remove disorder from the crystal lattice. Significant evidence for

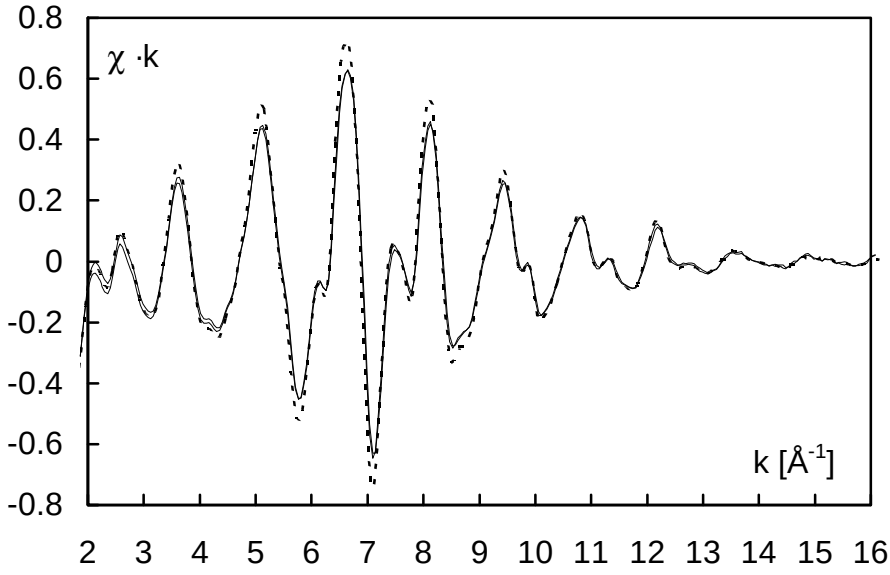

Figure 4.1.1. k^1-weighted EXAFS of 8 μm Ni foil measured in transmission (broken line) and of the Ni-wafer measured in TEY detection in its untreated state and after annealing at 400°C and 600°C (full lines).

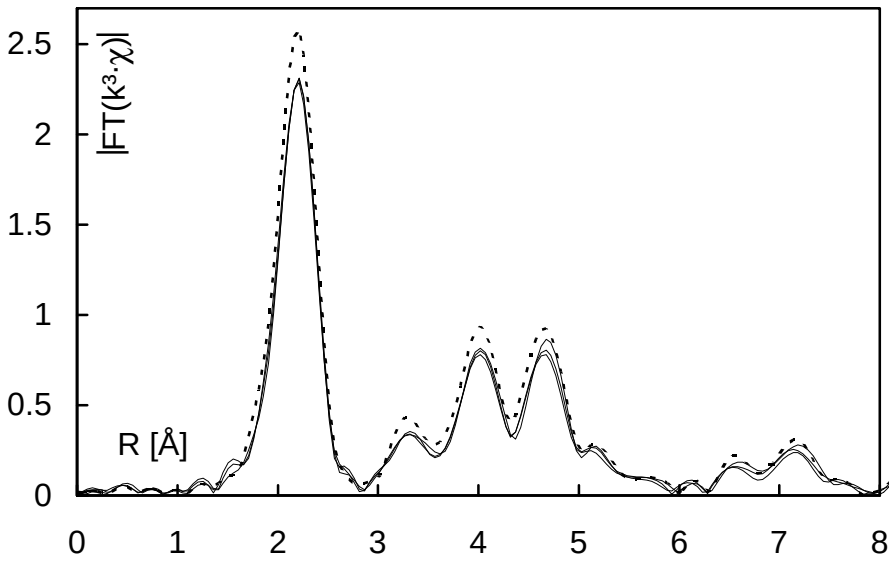

Figure 4.1.2. Modulus of the Fourier transforms of the spectra displayed in figure 4.1.1. (a k^3-weighting was applied before transformation). Broken line: Ni foil measured in transmission; full lines: TEY data of untreated Ni wafer and after annealing at 400°C and 600°C.

chemical reduction or lattice ordering is nevertheless absent in the TEY EXAFS data. The background subtracted, normalised TEY EXAFS functions of the Ni wafer are, within the noise level, indistinguishable (fig. 4.1.1). The same conclusion applies to the radial distribution functions obtained by Fourier transforming the spectra (fig. 4.1.2), and to the results of a multi-shell single scattering analysis using the curved-wave theory (table 4.1.1). Comparison with the transmission spectrum reveals a constant amplitude reduction of 18% ± 5% in the plots of the EXAFS (fig. 4.1.1) and the corresponding radial distribution functions (fig. 4.1.2).

The results of the fitting analysis with EXCURV92 (table 4.1.1) are also essentially identical for transmission and TEY data, except for the variation of the energy-independent amplitude factor S_0^2 (denoted AFAC in EXCURV92). This parameter was originally introduced into the curved-wave scattering theory to account for EXAFS amplitude losses due to multiple core-excitations (cf., chapter 1 and refs. [1,16]), and is expected to assume a value close to unity. In line with this, a value of 0.93 was obtained by the analysis of the transmission spectrum, but all TEY data are, within confidence limits, characterised by a reduced S_0^2 value of approximately 0.78. Closer inspection of the fitted Debye-Waller factors indicates a weak trend towards

Table 4.1.1. Analysis results for the unfiltered k^3-weighted Ni EXAFS data. The data were fitted over the k-range between 3 $Å^{-1}$ and 15 $Å^{-1}$. The coordination numbers N_i were held constant at the ideal values. The fitted fourth shell distance R_4 is too low because of a multiple-scattering effect. The same explanation applies to the anomalous Debye-Waller factors σ_2 and σ_4 for the second (value too high) and fourth (value too low) coordination shells. Each number in brackets denotes the statistical error-margin applying to the last digit of the preceding parameter.

	transmission	untreated	H_2 at 400°C	H_2 at 600°C
S_0^2	0.93 (3)	0.79 (3)	0.79 (3)	0.75 (3)
N_1, N_2,..., N_5		12, 6, 24, 12, 24 (ideal values, not fitted)		
R_1 [Å]	2.481 (1)	2.481 (2)	2.485 (2)	2.483 (2)
R_2 [Å]	3.506 (7)	3.498 (8)	3.504 (8)	3.506 (8)
R_3 [Å]	4.331 (3)	4.330 (4)	4.336 (4)	4.333 (4)
R_4 [Å]	4.822 (3)	4.818 (4)	4.824 (4)	4.825 (4)
R_5 [Å]	5.595 (9)	5.593 (10)	5.598 (9)	5.594 (10)
σ_1	0.0133 (4)	0.0131 (4)	0.0127 (4)	0.0122 (5)
σ_2	0.0183 (16)	0.0196 (18)	0.0192 (18)	0.0183 (19)
σ_3	0.0170 (7)	0.0175 (7)	0.0169 (7)	0.0161 (8)
σ_4	0.0082 (5)	0.0084 (6)	0.0077 (6)	0.0071 (6)
σ_5	0.0236 (21)	0.0237 (2)	0.0223 (21)	0.0218 (23)
R-factor [%]	25	23	24	26

increasing lattice order (lower factors) after higher reduction temperatures, but the variation is somewhat offset by a similar tendency to lower S_0^2 values. All parameter changes are still within the statistical error margins [17]. The amplitude information can therefore be regarded as identical for all three TEY spectra, confirming that 'near-surface disorder' is unlikely to be the cause of the reduced EXAFS amplitudes.

Examination of the near-edge region of the normalised spectrum reveals non-linearities in the TEY spectra (fig. 4.1.3) which are reminiscent of data obtained by fluorescence-yield measurements on inappropriately thick samples [9,18,19]. This suggests that the so-called 'self-absorption' effect which is well known to cause non-linear fluorescence-yield responses [18-24] might also be the origin of the distortions in the present TEY signal. It is interesting that Long *et al.* have already speculated about the existence of such a self-absorption correction for TEY data taken at grazing X-ray incidence [9]. Furthermore, TEY XAFS amplitude distortions are also visible in previously published TEY data recorded at glancing X-ray incidence near the critical angle for total reflection of light [25,26]. These observations suggest strongly that the linear response of the TEY signal breaks down at low incidence angles where the X-ray penetration of the sample approaches the escape depth of the signal

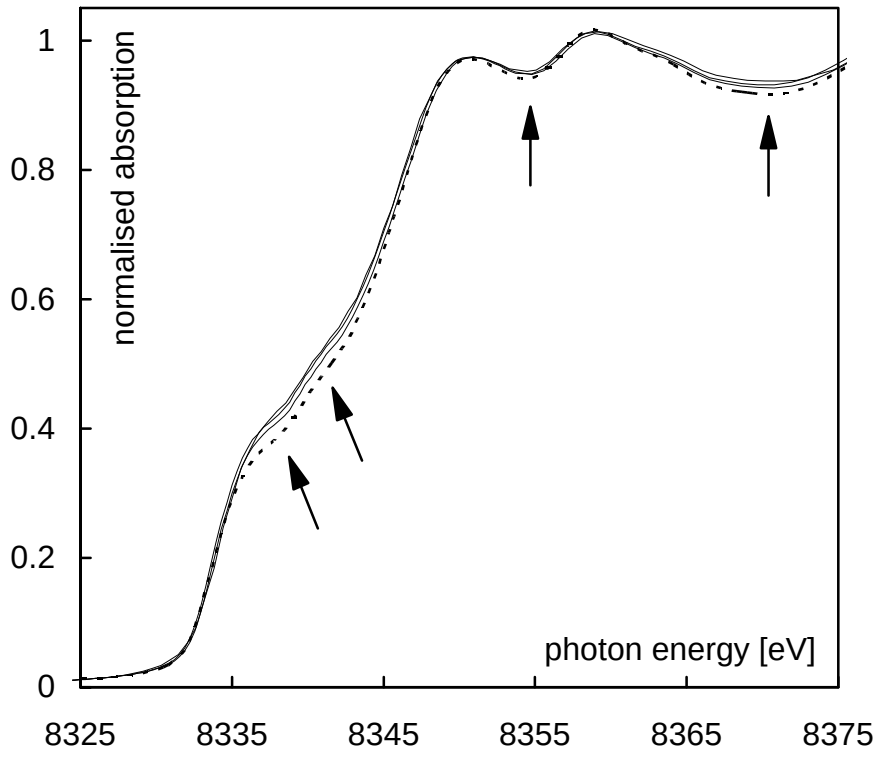

Figure 4.1.3. Near edge-region of the background subtracted, normalised spectra of the Ni foil (transmission, broken line) and the Ni wafers before and after the two annealing treatments (full lines). The arrows point to the regions where the non-linear deviations between the transmission and TEY spectra are most pronounced.

electrons. This effect will be discussed in more detail in section 4.2. where it will also be shown that the well-known theory of 'self-absorption' effects, previously developed for fluorescence-yield detection [18], can be employed to estimate the resulting TEY amplitude reduction factor *Dc(E) via*

$$\Delta c(E) \approx 100 \cdot \frac{\overline{m}(E)}{\overline{m}_{tot}(E) + l^{-1} \cdot \sin J} \ [\%], \qquad (4.1.1)$$

where $\overline{m}_{tot}(E)$ and $\overline{m}(E)$ refer to the smooth non-oscillatory parts of the total X-ray absorption coefficient $m_{tot}(E)$ and the contribution to $\overline{m}_{tot}(E)$ from the absorption edge step. The angle J is the angle of X-ray incidence with respect to the surface plane, and l an exponential attenuation parameter which describes the depth information contained in the TEY. The parameter l can be obtained using the Monte-Carlo simulation methods developed in chapter 3. The K-edge TEY signal in the present gas-flow experiment is mainly determined by the emission of Ni KLL electrons, and a best exponential fit to the results of a Monte-Carlo simulation of the Ni KLL emission into He yields a value of 353 Å for l (fig. 4.1.4). Using tabulated values for the X-ray absorption coefficients $\overline{m}_{tot}(E)$ and $\overline{m}(E)$ [27], eq. (4.1.1) thus predicts an EXAFS amplitude reduction of approximately 9% for the incidence angle of 5° (fig. 4.1.5). Applying this correction to the TEY EXAFS data of the Ni wafer results in much better agreement with the transmission results (figure 4.1.6).

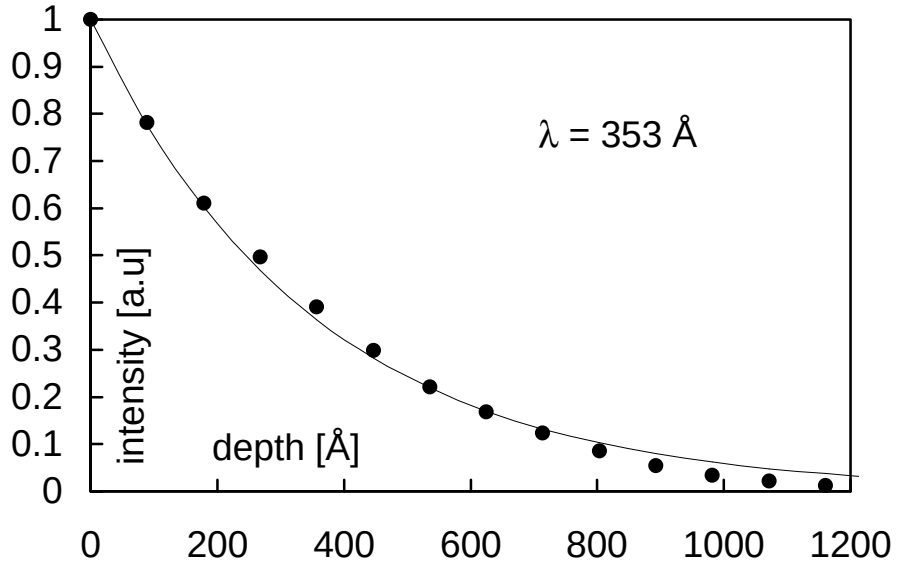

Figure 4.1.4 Depth information carried by the Ni KLL signal (6.5 keV) emitted from a Ni surface into He, as calculated by Monte-Carlo simulations of electron trajectories (black circles). The line represents an exponential attenuation function with an attenuation constant of 353 Å.

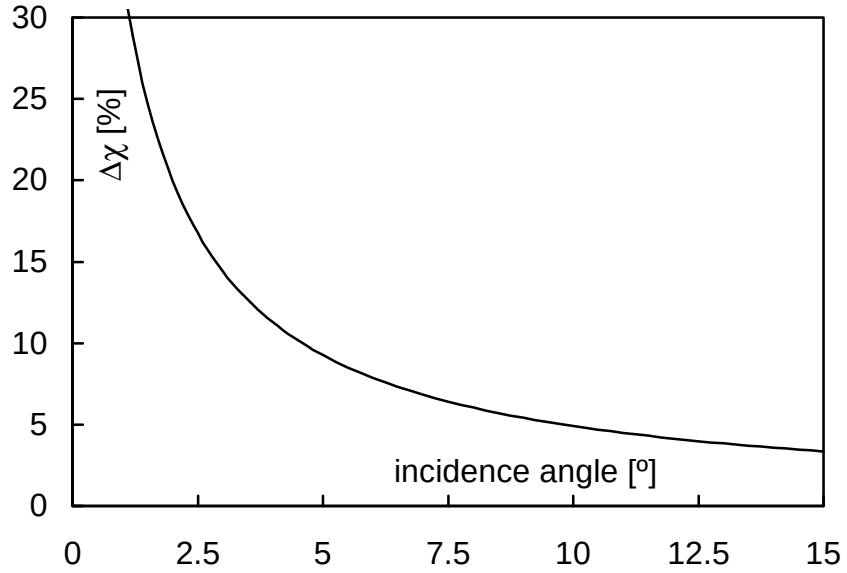

Figure 4.1.5 Calculated TEY EXAFS amplitude reduction for Ni metal as a function of incidence angle. Parameters: $\overline{m}_{tot}(E)$ = 329.2 cm^2/g, $\overline{m}(E)$ = 287.4 cm^2/g, l = 353 Å.

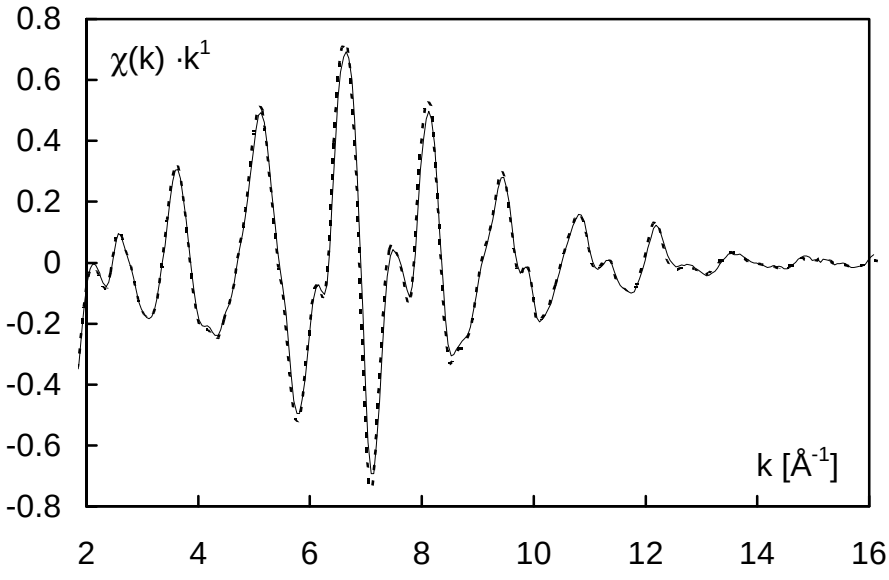

Figure 4.1.6 Corrected, k^1-weighted TEY EXAFS of the untreated Ni wafer (full full line) compared to the EXAFS of the 8 μm Ni foil measured in transmission (broken line).

A normal-incidence TEY spectrum of a similar Ni sample (data presented in Appendix B) confirms the prediction of eq. (4.1.1) that the deviations between TEY and transmission data of Ni should be smaller for non-grazing X-ray incidence. This result will be discussed in more detail in section 4.2. Further TEY investigations of Ni metal have been described in refs. [4,6,28], but direct comparison with the results of these studies is made difficult by the fact that thin Ni foils were investigated,

which may exhibit different amplitude characteristics. Furthermore, the strong amplitude reductions observed in [6] should be interpreted with caution, as the TEY signal also exhibited a strong dependence on the polarity of the collector bias voltage. This indicates that the detector response was non-linear, possibly because the electric field in the detector was non-uniform due to insufficient gas-flow (such effects have been observed by the author during his own experiments). The EXAFS spectra given in [4] are much more in line with the results found by the present study and in ref. [28]. Taking the evidence together, it seems likely that a 'self-absorption' effect explains the EXAFS amplitude reductions which have previously been reported for TEY experiments at low angles of incidence [1,7,9].

It should be noted, however, that the correction calculated with equation (4.1.1) still underestimates the experimentally determined amplitude reduction for Ni by a few percent (cf. table 4.1.1). Other TEY data reported in the literature also indicate that reduced EXAFS amplitudes exist, at least for some materials, even at normal X-ray incidence [3-5]. The origin of the non-linear TEY response in these experiments remains unexplained. The most important contribution, to be discussed in section 4.3, is due to photoelectrons excited by fluorescent photons. This photoelectron fraction of the TEY can become significant when optically dense materials with high fluorescence-yields are investigated. The morphology of the sample might also influence the response of the TEY signal to the X-ray absorption coefficient. In particular powders and samples with high surface roughness should be relatively insensitive to the grazing-incidence 'self-absorption' effect because an average orientation of the facets exposed by the crystallites is being probed. Furthermore, evidence (to be presented in chapter 5) has been found which indicates that exposure of dispersed metals to small amounts of corrosive gases, including air, can result in reduced XAFS amplitudes. A combination of several causes can explain why reduced TEY amplitudes are not omnipresent (cf., e.g., results in refs. [4,29] which indicated that TEY and transmission data are identical).

The main conclusion derived from the *in situ* annealing measurements is that 'near-surface disorder' is not the sole explanation for reduced TEY EXAFS amplitudes. Significant amplitude deviations due to a 'self-absorption' effect are expected at X-ray incidence angles below 10° with respect to the surface plane. A more detailed study of this effect will now be described.

4.2. 'Self-Absorption' Correction for Total Electron-Yield X-ray Absorption Fine Structure Amplitudes Detected at Grazing Incidence Angles

4.2.1. Introduction

Since the early days of X-ray absorption spectroscopy (XAS) it has been known that sample inhomogeneities [30] or spectral impurities in the exciting X-ray beam [31] can be the source of non-linearities in transmission measurements of the absorption coefficient. Because the magnitude of the resulting XAFS amplitude distortions increases with the thickness of the sample the phenomenon is often referred to as the 'thickness effect' [32]. Knowledge of its origin has enabled the prediction of the experimental conditions under which thickness effects are minimised [32-34]. Fluorescence-yield detection, introduced for XAS measurements in the late 1970s [35], suffers from similar non-linearities which occur because the absorption cross section for fluorescent photons is typically an order of magnitude smaller than for the incident X-radiation (*vide infra*). The resulting absorption length difference leads to a non-linear response of the fluorescence signal when optically dense and/or thick samples are investigated [18-22,36]. It has been shown that the amplitude reduction introduced by this 'self-absorption' effect can be corrected during data analysis provided that sample composition, sample density, and the X-ray absorption coefficients of the constituent elements are known [18-24].

As already mentioned in section 4.1.1, the factors which cause amplitude reductions in TEY spectra are much less understood. Reports of the first electron-yield measurements date back more than two decades [37], but surprisingly little attention has been paid to the unrealistically small XAFS amplitudes which have been observed in several TEY studies [4-6,8,9,38-40]. Some authors have recently gone so far as to state that 'self-absorption'-like amplitude distortions are absent from TEY data [29,41-44]. The reduced XAFS amplitudes found in several experimental studies suggest that this statement is too strong. In section 4.1. it was argued that 'near-surface disorder', previously invoked as the explanation for amplitude distortions in TEY spectra, is not the explanation for the reduced XAFS amplitudes observed for grazing-incidence measurements on optically flat Ni samples. The present section describes a more systematic study of the relation between the X-ray incidence angle and the TEY XAFS amplitude. Three different samples were investigated, including a Cr single crystal, a polycrystalline Ni wafer and the pressed pellet of a powdered compound (ZnO). It will be shown that the grazing-incidence 'self-absorption' effect is a general feature in TEY detection. How the dependence on sample composition

and fluorescence-yield intensity can be predicted quantitatively, will also be demonstrated.

4.2.2. Experimental

Experiments were carried out on station 8.1 at daresbury Laboratory with the electron storage ring in Daresbury (U.K.) operating with beam currents of 190 ± 50 mA. Most details of the measurements were as described in section 4.1.2. The incident X-ray flux was monitored with an ion chamber filled with the appropriate mixtures of Ar and He to result in an absorption of 20% at all absorption edges. All measurements were carried out in the combined vacuum/gas-flow cell described in section 2.5. The cell was fitted with a single-axis rotary feedthrough allowing sample orientation between 0° and 180° with respect to the beam. The scale of the rotary drive was calibrated at the beamline, with the cell mounted on the optical bench. A laser was carefully aligned along the beampath of the X-rays. The normal-incidence position of the sample was determined as the position at which the laser beam reflected from the sample traced back its incoming path. The accuracy of the sample orientation derived by this method was within ± 0.5°. The precision of the rotary drive was within ± 0.2°. All samples were mounted on a purpose-built Ta foil (thickness 0.5 mm) support, which was attached to a 1 mm diam. stainless-steel extension to the rotary drive. Electrical insulation between the stainless steel rod and the feedthrough was maintained by a small acetal homopolymer (Delrin) shaft. Electrical connection to the sample was made by a thin Ta wire spotwelded to the stainless steel extension. Samples were fixed onto the Ta support with a system of 0.1 mm Ta wires. Free sample rotation excluded the use of a positively biased counterelectrode for maintenance of an electrical field in the detector. In contrast to all other measurements reported in this thesis, a *negative* detector bias was therefore placed *on the sample* (-104 V, commercial batteries). The TEY current through the batteries was measured with a Keithley preamplifier. The grounded cell acted as the counterelectrode. Samples included Cr, Ni and ZnO. The Cr sample was a diamond-polished (final grain size: 0.1 μm) single crystal specimen (ellipsoidal shape, average diameter approximately 1 cm, thickness 0.8 mm) covered by its native room temperature oxide overlayer. By sputter depth profiling and oxide growth experiments under controlled (ultra-high vacuum) conditions, using low-energy electron diffraction and Auger electron spectroscopy, the thickness of this oxide layer was determined to be less than 30 Å, a result which is in agreement with earlier studies [45-59]. A diamond polished (final grain size: 0.5 μm) polycrystalline Ni specimen analogous to those described in section 4.1.2. was used as the Ni sample.

ZnO (Fisons AR, 99.5%) was investigated in the form of a pellet of ZnO (diameter: 1.4 cm) produced by pressing at 15 t in a die with diamond-polished surfaces. The resulting sample specimen was shiny, with a high reflectivity for visible light.

Unfortunately, the Cr sample was too small to give reliable results at incidence angles below 5°. Below this angle, the incident X-ray beam did not only trace the sample but also internal stainless-steel parts of the gas-flow cell, as indicated by the appearance of a Fe K-edge signal at 7100 eV. Contamination of the electron-yield signal by Cr present in stainless-steel could not be excluded so that measurements at incidence angles below 5° were not performed. Similar problems did not occur with the Ni (large enough to attenuate the beam completely) and the ZnO sample (Zn not present in the cell environment).

4.2.3. Results

A representative selection of raw near-edge and EXAFS spectra is given in fig. 4.2.1. Significant amplitude distortions at low angles of incidence are seen for all three materials, but the most pronounced deviations are seen for Ni. It is interesting that the ZnO sample does actually exhibit the angular anisotropy of the TEY signal, as this indicates that pressing of a pellet produces a sample with sufficiently small microroughness to induce the 'self-absorption' effect. The effect should be absent or reduced for samples with rough surfaces because the effective incidence angle is non-grazing, as it is angle-averaged over all crystallite facets exposed to the beam. The presence of the 'self-absorption' effect in the ZnO spectra thus indicates that the pellet surface is smooth on a scale which corresponds to incidence angle variations of less than a few percent. The ZnO results demonstrate for the first time that the 'self-absorption' correction at grazing incidence is not only limited to metallic samples.

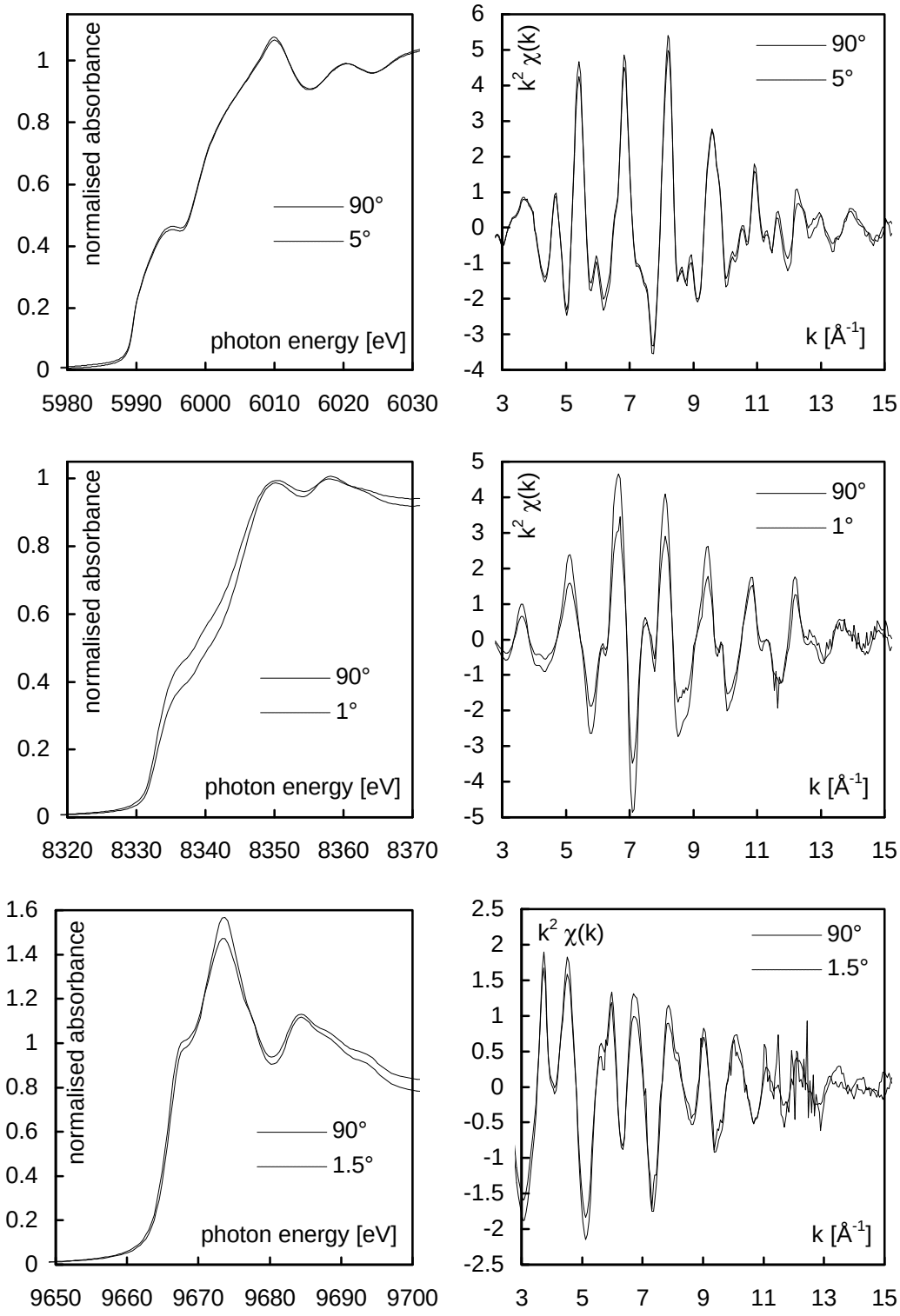

Figure 4.2.1. TEY K-edge spectra of a polished Cr single crystal (top row), a polished, polycrystalline Ni wafer (middle row) and a pellet of ZnO (bottom row) measured at normal (90°, full lines) and grazing X-ray incidence (exact angles given in diagram, broken lines). The near-edge (left column) and the EXAFS regions (right column) of the grazing incidence data exhibit 'self-absorption' distortions. The large noise 'spikes' at k-values between 11 $Å^{-1}$ and 13 $Å^{-1}$ in the grazing incidence data for ZnO are related to Bragg reflections in the Si(220) monochromator crystals.

The magnitude of the amplitude reductions in the data at non-normal incidence was quantified by determining the energy-independent scaling factor A which afforded best least-squares agreement with the TEY EXAFS spectrum of the same sample taken at normal incidence. The k-region fitted for the analysis was from 3 Å^{-1} to 15 Å^{-1} for Cr and Ni, and from 3 Å^{-1} to 13 Å^{-1} for ZnO. No k-weighting of the spectra was applied during this analysis. The EXAFS amplitude reduction $\Delta\chi$ is given by $\Delta c = 1 - 1/A$. Representative results of the least-squares fitting procedure are presented in figure 4.2.2.

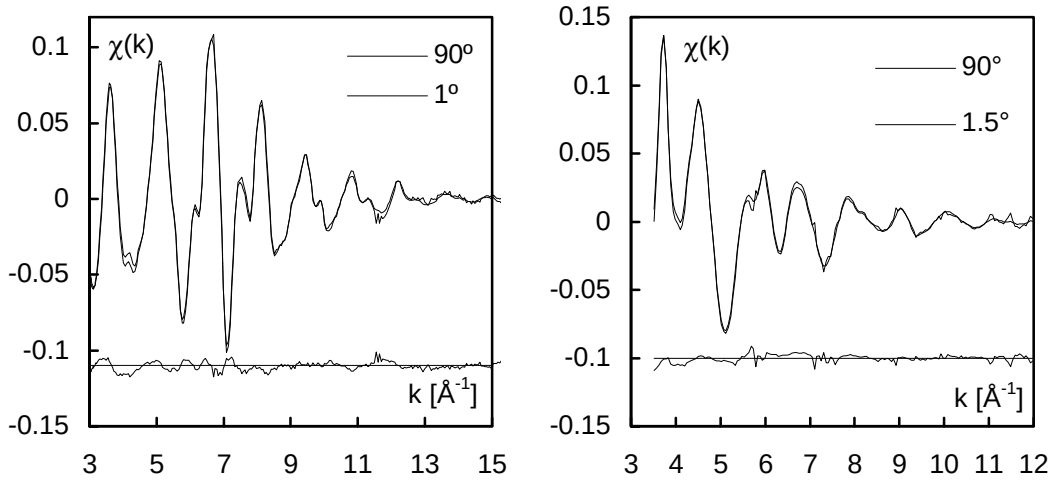

Figure 4.2.2. Results of the data analysis described in the text. The grazing incidence spectra of Ni and ZnO from fig. 4.2.1 have been scaled by a k-independent factor to achieve a best least-squares fit with the normal incidence reference TEY spectrum. The resulting difference spectra are plotted with a negative offset to the data.

Choosing the normal incidence TEY spectrum as the reference eliminates the influence of angle *independent* amplitude distortions in the TEY signal. This is important, because the normal-incidence TEY spectra are additionally reduced due to photoelectron contributions excited by fluorescent photons and/or disorder in the near-surface region of the sample.

4.2.4. Model Calculations

(i) Pre-edge region - The emitted flux of electrons in the pre-edge region is determined by photoemission from all atomic levels with binding energies below the absorption edge energy. Any amplification of the photoelectron signal *via* secondary electron production will be neglected, in line with the conclusion of section 3.4. that the cross sections for secondary electron excitation by keV electrons are small. TEY data in the soft X-ray range might have to be analysed with a more sophisticated model which accounts for secondary charges. For gas-flow TEY detection, the

neglect of secondary electrons is always justified, as gas-phase ionisation events amplify the photoelectron channel strongly.

The magnitude of the pre-edge absorption coefficient is typically 5% - 20% of the post-edge value [27,60,61] and is dominated by the cross section for photoionization of the core level which corresponds to the absorption edge closest on the low-energy side of the edge of interest. This is the situation which applies to the largest body of experimental TEY data reported in the literature, *i.e.* K- and L_{III}-edge experiments on elemental samples. The pre-edge signal is stronger in the case of L_I- and L_{II}-edge spectra, because the presence of other L-edges in the pre-edge region contributes a large background signal, often exceeding the magnitude of the signal of the investigated edge. Similarly, samples containing several elements (compounds, heterogeneous mixtures or layered structures) might exhibit an absorption edge close to the pre-edge region. The various contributions to the pre-edge signal can always be calculated from tabulated absorption cross sections [27,60,61], provided that the elemental composition and density of the sample are known.

(ii) Absorption edge and post-edge region - The edge-step and post-edge TEY signals have their origin in the emission of energetic Auger electrons during the neutralisation of the X-ray induced core vacancies. The TEY current from the edge of interest is dominated by the primary and secondary Auger electrons which are, respectively, emitted in the first and second Auger transitions after the photoelectric core hole creation [4]. For K- and L-edges, the number of primary Auger electrons can be derived from tabulated values [62] for the KLL and LMM transition probabilities. The number of Auger electrons from the secondary decay step (LMM in the case of K-edge experiments, MNN for L-edge experiments) is similarly derived (see section 2.5). Any TEY contributions due to secondary electron production will be ignored. The small contribution of photoelectrons excited from the core level which is responsible for the absorption edge of interest will also be neglected.

(iii) Depth information in Auger electron channel - The analysis of the experimental data acquired for Cr, Ni, and ZnO will be carried out using the results of Monte-Carlo electron trajectory simulations. To investigate general trends throughout the periodic system, a ‘universal curve’ similar to that presented in section 3.10 will be employed. The universal expression deduced in 3.10 itself cannot be used because the calculations of the grazing-incidence ‘self absorption’ effect are based on an exponential depth distribution function for the Auger electron trajectories. The 40

depth distribution functions from section 3.10 have therefore been fitted with the exponential function [63]:

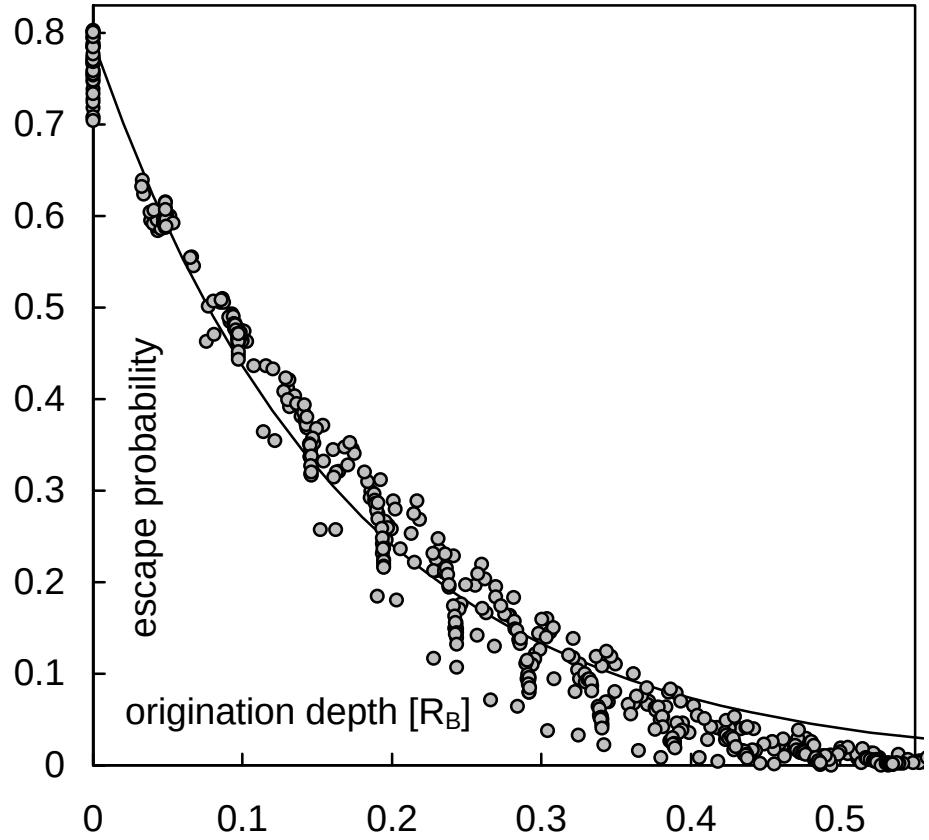

Figure 4.2.3. 'Universal' exponential depth distribution function given by eq. (4.2.1).

$$P(x) = 0.79 \cdot \exp(-5.94 \cdot x / R_B) = 0.79 \cdot \exp(-x / l) \qquad (4.2.1)$$

which represents a best least-squares fit to the collection of datapoints up to 0.4 R_B (fig. 4.2.3). Small deviations from exponential attenuation are seen, especially at electron origination depths above 0.4 R_B where the exponential law predicts larger electron-yield currents than the Monte-Carlo simulations. However, the longer 'tail' of the exponential function compensates for an important shortcoming of the Monte-Carlo simulations, *i.e.* the neglect of straggling and photoelectrons excited by the fluorescence-yield, which enhance the information from larger depths in the sample. It should also be kept in mind that the error introduced by assuming an exponential attenuation law might well be offset by uncertainties related to other simplifications made in the Monte-Carlo simulation analysis.

4.2.5. Calculation of the Grazing Incidence 'Self-Absorption' Effect

It is assumed that the size of the sample is much larger than the size of the incident beam, and that the atomic X-ray absorption cross section and electron emission rates are both isotropic in angle. The TEY is dominated by three contributions: the pre-edge photoelectron signal $I_{ph}(E)$ and the Auger electron signals $I_p(E)$ and $I_S(E)$ from the primary and secondary Auger decay. Let J be the angle of X-ray incidence with respect to the sample surface plane and $l(E_i)$ the attenuation length for the electrons of kinetic energy E_i. Then the three signals $dI_i(E,x)$ deriving from a depth dx can be expressed as

$$dI_{ph}(E,x) \propto \frac{m_{ph}(E)}{\sin J} \cdot I_0(E) \cdot \exp\left(-\left(\frac{m_{tot}(E)}{\sin f} + l^{-1}(E_{ph})\right) \cdot x\right) \cdot dx, \quad (4.2.2a)$$

$$dI_{p}(E,x) \propto \frac{m(E) \cdot a_p}{\sin J} \cdot I_0(E) \cdot \exp\left(-\left(\frac{m_{tot}(E)}{\sin f} + l^{-1}(E_{p})\right) \cdot x\right) \cdot dx, \quad (4.2.2b)$$

$$\begin{aligned} dI_{s}(E,x) \propto \frac{m(E)}{\sin J} \cdot \left(2a_p a_s + \frac{w_p \cdot a_s}{1+K}\right) \cdot \ldots \\ \ldots I_0(E) \cdot \exp\left(-\left(\frac{m_{tot}(E)}{\sin f} + l^{-1}(E_{s})\right) \cdot x\right) \cdot dx \end{aligned}, \quad (4.2.2c)$$

where $I_0(E)$ is the incident photon flux at energy E, $m(E)$ the absorption coefficient for the absorption edge of interest, $m_{ph}(E)$ the absorption coefficient for photoelectron excitation in less tightly bound atomic levels, a_p and a_s the probabilities for non-radiative decay [62] of the primary and secondary core vacancies, w_p the probability for fluorescent decay of core holes produced at the edge [62], and K the factor accounting for relative X-ray emission rates [64]. The total absorption cross section $m_{tot}(E)$ will now be approximated by

$$m_{tot}(E) \approx m(E) + m_{ph}(E) \quad (4.2.3)$$

and determines, together with the angle of incidence J, the X-ray intensity in the sample region dx. Integration of the three expressions over the sample thickness d yields the normalised emission currents:

$$\frac{I_{ph}(E)}{I_0(E)} \propto \frac{m_{ph}(E)}{m_{tot}(E) + l^{-1}(E_{ph}) \cdot \sin J} \cdot \ldots \cdot \left(1 - \exp\left(-\left(\frac{m_{tot}(E)}{\sin J} + l^{-1}(E_{ph})\right) \cdot d\right)\right), \quad (4.2.4a)$$

$$\frac{I_p(E)}{I_0(E)} \propto \frac{m(E)}{m_{tot}(E) + l^{-1}(E_p) \cdot \sin J} \cdot a_p \cdot \ldots \cdot \left(1 - \exp\left(-\left(\frac{m_{tot}(E)}{\sin J} + l^{-1}(E_p)\right) \cdot d\right)\right), \quad (4.2.4b)$$

$$\frac{I_s(E)}{I_0(E)} \propto \frac{m(E)}{m_{tot}(E) + l^{-1}(E_s) \cdot \sin J} \cdot \left(2a_p a_s + \frac{w_p \cdot a_s}{1+K}\right) \cdot \ldots \cdot \left(1 - \exp\left(-\left(\frac{m_{tot}(E)}{\sin J} + l^{-1}(E_s)\right) \cdot d\right)\right). \quad (4.2.4c)$$

For a sufficiently thick sample the exponential term approaches zero, and the expressions reduce to:

$$\frac{I_{ph}(E)}{I_0(E)} \propto \frac{m_{ph}(E)}{m_{tot}(E) + l^{-1}(E_{ph}) \cdot \sin J}, \quad (4.2.5a)$$

$$\frac{I_p(E)}{I_0(E)} \propto \frac{m(E)}{m_{tot}(E) + l^{-1}(E_p) \cdot \sin J} \cdot a_p, \quad (4.2.5b)$$

$$\frac{I_s(E)}{I_0(E)} \propto \frac{m(E)}{m_{tot}(E) + l^{-1}(E_s) \cdot \sin J} \cdot \left(2a_p a_s + \frac{w_p \cdot a_s}{1+K}\right). \quad (4.2.5c)$$

The correction factor in the brackets of the last equation was first determined by Erbil *et al.* [4] and is a generalisation of the factor n_{LMM} defined by eq. (3.5) in chapter 3. The TEY contribution of $I_s(E)$ is about an order of magnitude lower than that of $I_p(E)$. The reason for this is that the attenuation length $l(E_s)$ is much shorter than $l(E_p)$ due to the large difference between the two Auger electron energies ($E_s \ll E_p$). For vacuum detection, the contribution of $I_s(E)$ is nevertheless often significant and should be accounted for when the 'self-absorption' effect at grazing incidence is analysed. For gas phase detection, the TEY contribution of $I_s(E)$ is comparatively small so that the absorption edge signal is well described by eq. (4.2.5b). The

mathematical form of this equation is analogous to the fundamental expression used for the derivation of the 'self-absorption' effect in fluorescence yield detected XAFS spectra of thick samples. More explicitly, the relevant equation for the fluorescence-yield is [18,21,22,35,65-67]

$$\frac{I_p(E)}{I_0(E)} \propto w_p \cdot \frac{m(E)}{m_{tot}(E) + m_{tot}(E_f) \cdot \sin J / \sin q} \qquad (4.2.6)$$

where q is the photon detection angle with respect to the sample surface and $m_{tot}(E_f)$ the absorption coefficient for the fluorescence.

Eqs. (4.2.5b) and (4.2.6) provide some insight into the circumstances under which significant 'self absorption' effects occur in any (fluorescence- or electron-) yield experiment. The ultimate goal of yield detection is to achieve proportionality to the absorption coefficient $m(E)$. However, eqs. (4.2.5b) and (4.2.6) show that the measured yield signal contains the total absorption coefficient $m_{tot}(E)$ in the denominator, and therefore, cf. eq. (4.2.3), also the edge absorption coefficient $m(E)$. The yield signals are only an accurate representation of the true absorption coefficient $m(E)$ when the second term in the denominator is sufficiently large compared to $m_{tot}(E)$. Taking an idealised case, in the absence of any pre-edge absorption ($m_{ph}(E) \approx 0$) and for negligible self-attenuation of the detected signal fluorescence ($m_{tot}(E_f) \approx 0$) or the Auger electron current ($l^{-1}(E_p) \approx 0$), the measured absorption spectrum would be featureless. The commonly used way to ascertain the proportionality between the fluorescence-yield signal and the absorption coefficient $m(E)$ is to dilute the sample sufficiently so that $m_{tot}(E_f)$ becomes large compared to $m(E)$. The TEY response to $m(E)$ is usually close to linearity even for optically dense (large absorption coefficient $m(E)$) materials because $l^{-1}(E_p)$ exceeds $m_{tot}(E)$ usually by one or two orders of magnitude. However, because of the additional influence of the incidence angle, non-linearities exist for grazing X-ray incidence where the influence of $\sin J$ reduces the second term in the denominator significantly.

Starting from eq. (4.2.6), Goulon *et al.* [18] (and, subsequently, other authors [19-23]) have shown that the experimental EXAFS amplitude in fluorescence-yield data of infinitely thick samples can be expressed as

$$c_{expt}^{flu}(E) \approx c(E) \cdot \left(1 - \frac{\overline{m}(E)}{\overline{m}_{tot}(E) + \overline{m}_{tot}(E_f) \cdot \sin J / \sin q}\right) = c(E) - \Delta c^{flu}, \qquad (4.2.7)$$

where c and c_{expt} are the physically correct and the experimentally determined EXAFS, respectively. $\overline{m}_{tot}(E)$, $\overline{m}(E)$ and $\overline{m}_{tot}(E_f)$ refer to the smooth non-oscillatory parts of (i) the total X-ray absorption coefficient $m_{tot}(E)$ at energy E, (ii) the contribution to $\overline{m}_{tot}(E)$ from the edge of interest, and (iii) the absorption coefficient $\overline{m}_{tot}(E_f)$ for the fluorescent photons of energy Ef. The angles J and q are the angles of X-ray incidence and fluorescence emission with respect to the surface plane. Because the smooth, 'atomic' absorption coefficients vary comparatively little in the post-edge region $Dc(E)$ can, in a good approximation, be regarded as energy-independent. This explains why constant scaling factors afforded good agreement between the EXAFS amplitude of the grazing- and normal incidence data. The corresponding expression for the energy-independent amplitude reduction Dc in the TEY signal reads

$$c_{expt}(E) \approx c(E) \cdot \left(1 - \frac{\overline{m}(E)}{\overline{m}_{tot}(E) + l^{-1}(E_p) \cdot \sin J} \right) \approx c(E) - \Delta c \,. \qquad (4.2.8)$$

The only modification to the expression for the fluorescence-yield stems from the fact that the dependence on the exit angle q is lost. The angular variation in q arises for fluorescence detection because photons propagate along a straight path through the sample, resulting in longer pathlengths for more grazing exit angles. In contrast, the motion of electrons is randomised by elastic and inelastic scattering events. The factor $\overline{m}_{tot}(E_f)/\sin q$ in eq. (4.2.7) is therefore replaced in eq. (4.2.8) by the q-independent exponential attenuation length $l^{-1}(E_p)$.

Using eq. (4.2.1) and tabulated values for the relevant X-ray absorption coefficients [27,61], Dc has been calculated for the K-edges of 31 elements and 9 transition metal oxides. The results are summarised in table 4.2.1. At first sight, it might appear surprising that Dc varies very little within the group of 31 elements, despite the fact that the corresponding K-edge energies span a substantial X-ray energy range from 1 keV to 30 keV. However, the material- and energy dependence of the attenuation characteristics for photons and electrons exhibit sufficient proportionality to ensure that most variations do cancel out. For compounds, such as the 9 oxides, the variations are much larger due to material density and electronic structure changes.

Table 4.2.1 Calculated total KLL-yield amplitude reduction $Dc = Dc(E_0)$ for 31 elements and 9 oxides for 5 different angles J of X-ray incidence. The first three columns give the calculation parameters used for the evaluation of eq. (4.2.8).

	$l(E_p)$	$\overline{m}_{tot}(E_0)$	$\overline{m}(E_0)$	$Dc(E_0)$ [%]				
	[Å]	[cm²/g]	[cm²/g]	J = 45°	J = 30°	J = 10°	J = 5°	J = 3°
Na	163	7789	7280	1.6	2.2	6.2	11.6	17.8
Mg	117	6003	5563	1.6	2.2	6.1	11.4	17.5
Al	103	4150	3591	1.4	2.0	5.4	10.1	15.6
Si	145	3396	3097	1.5	2.0	5.7	10.6	16.4
K	1130	1307	1173	1.6	2.2	6.1	11.4	17.6
Ca	729	1073	953.6	1.5	2.1	5.8	10.9	16.7
Sc	479	854.0	755.8	1.5	2.1	5.8	10.9	16.8
Ti	378	712.8	629.2	1.5	2.1	5.8	10.9	16.7
V	334	602.7	532.1	1.5	2.1	5.8	10.9	16.8
Cr	323	517.7	454.0	1.5	2.1	5.7	10.6	16.4
Mn	366	454.9	397.8	1.5	2.1	5.8	10.9	16.7
Fe	389	408.4	357.5	1.5	2.1	5.9	11.0	16.9
Co	400	350.1	306.2	1.5	2.1	5.9	10.9	16.8
Ni	438	329.2	287.4	1.6	2.2	6.0	11.2	17.2
Cu	516	283.4	247.2	1.6	2.2	6.1	11.4	17.5
Zn	728	260.5	227.3	1.6	2.3	6.3	11.7	17.9
Ga	1017	221.0	192.0	1.6	2.2	6.2	11.5	17.6
Ge	1274	201.3	175.0	1.6	2.3	6.3	11.8	18.0
As	1321	179.8	164.2	1.7	2.4	6.6	12.3	18.8
Rb	7334	128.8	110.8	1.7	2.4	6.6	12.2	18.6
Sr	4890	109.3	93.5	1.6	2.3	6.2	11.5	17.6
Y	3667	101.9	87.1	2.0	2.8	7.5	13.7	20.6
Zr	2397	94.7	80.7	1.7	2.5	6.7	12.4	18.8
Nb	1908	87.5	74.6	1.7	2.4	6.5	12.0	18.3
Mo	1760	80.8	68.9	1.7	2.4	6.6	12.2	18.5
Ru	1729	68.1	57.5	1.7	2.4	6.6	12.1	18.4
Rh	1862	63.4	53.6	1.7	2.4	6.6	12.2	18.5
Pd	2106	58.1	48.9	1.7	2.4	6.6	12.2	18.5
Ag	2445	54.9	45.9	1.6	2.3	6.3	11.6	17.7
Cd	3456	50.5	42.6	1.8	2.5	6.7	12.5	18.9
In	4410	46.9	39.4	1.8	2.5	6.7	12.4	18.8
TiO_2(r)	312	443.8	374.2	0.68	1.0	2.7	5.2	8.4
TiO_2(a)	318	443.4	373.3	0.68	1.0	2.7	5.2	8.4
Cr_2O_3	351	362.8	311.2	0.80	1.1	3.2	6.1	9.7
CrO_2	365	329.8	280.4	0.70	1.0	2.8	5.4	8.6
Fe_2O_3	466	290.5	250.7	0.86	1.2	3.4	6.5	10.3
NiO	488	260.7	225.3	1.02	1.4	4.0	7.7	12.1
Cu_2O	668	252.1	218.7	1.22	1.7	4.8	9.0	14.0
CuO	601	225.6	195.3	1.05	1.5	4.1	7.8	12.3
ZnO	772	209.4	181.3	1.10	1.5	4.3	8.2	12.8

4.2.6. Comparison of Calculated and Experimental Results

Values for $l(E_p)$ for Cr, Ni and ZnO were derived by Monte-Carlo simulations of the KLL electron trajectories *including the amplifying effect of the gas-phase* as described in section 3.7. The modified depth distribution functions derived by these simulations are presented in figure 4.2.4 together with the best exponential fits, which can be seen to be a good representation of the depth information in the gas-flow KLL signal. Using the exponential decay constants derived from the fits and literature values for the absorption coefficients [27], the self-absorption correction *Dc* was calculated using eq. (4.2.8). All calculated and experimental results are coplotted in figures 4.2.5. - 4.2.7.

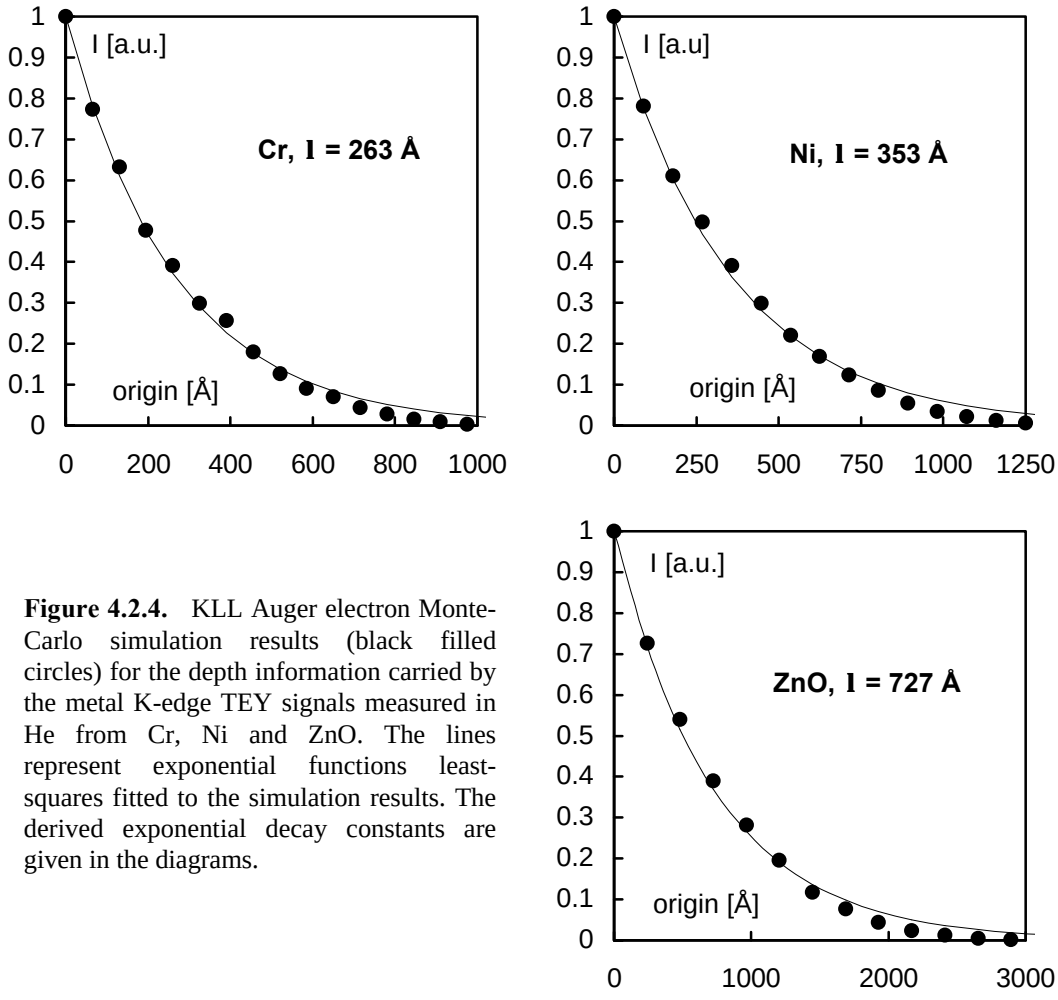

Figure 4.2.4. KLL Auger electron Monte-Carlo simulation results (black filled circles) for the depth information carried by the metal K-edge TEY signals measured in He from Cr, Ni and ZnO. The lines represent exponential functions least-squares fitted to the simulation results. The derived exponential decay constants are given in the diagrams.

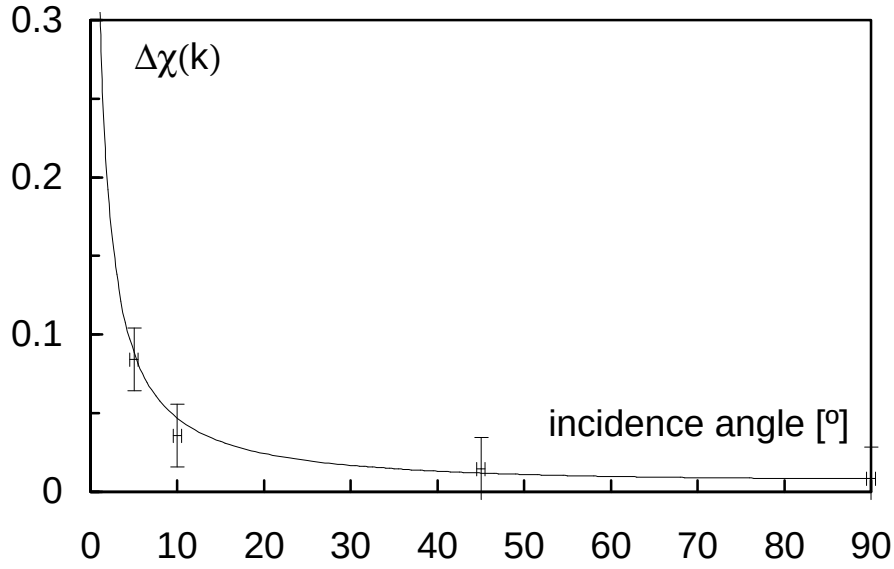

Figure 4.2.5. Experimental data for a polished Cr(110) single crystal specimen compared to the predictions of eq. (4.2.8). Calculation parameters: l = 263 Å, $\overline{m}_{\mathrm{tot}}(E)$ = 517.7 cm^2/g, $\overline{m}(E)$ = 454 cm^2/g, density = 7.19 g/cm^3.

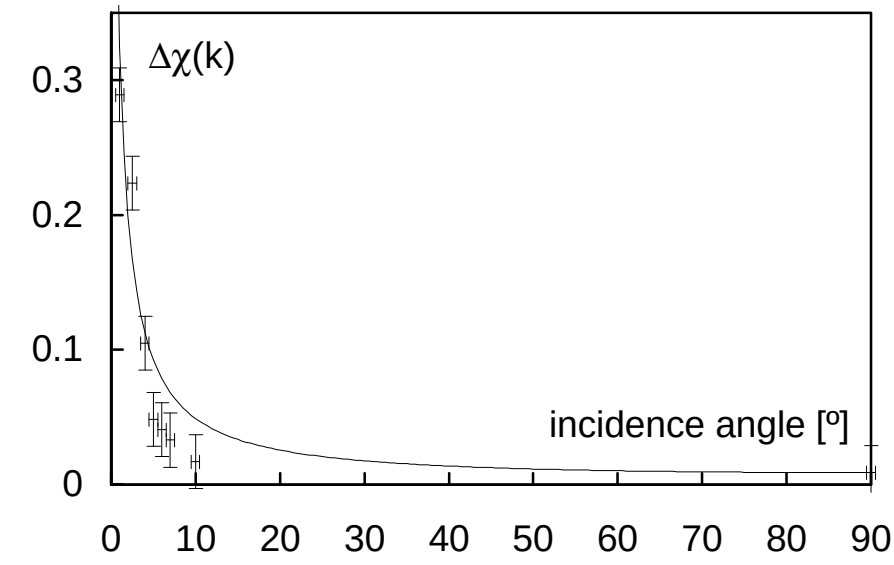

Figure 4.2.6. Experimental data for a polished polycrystalline Ni specimen compared to the predictions of eq. (4.2.8). Calculation parameters: l = 353 Å, $\overline{m}_{\mathrm{tot}}(E)$ = 329.2 cm^2/g, $\overline{m}(E)$ = 287.4 cm^2/g, density = 8.90 g/cm^3.

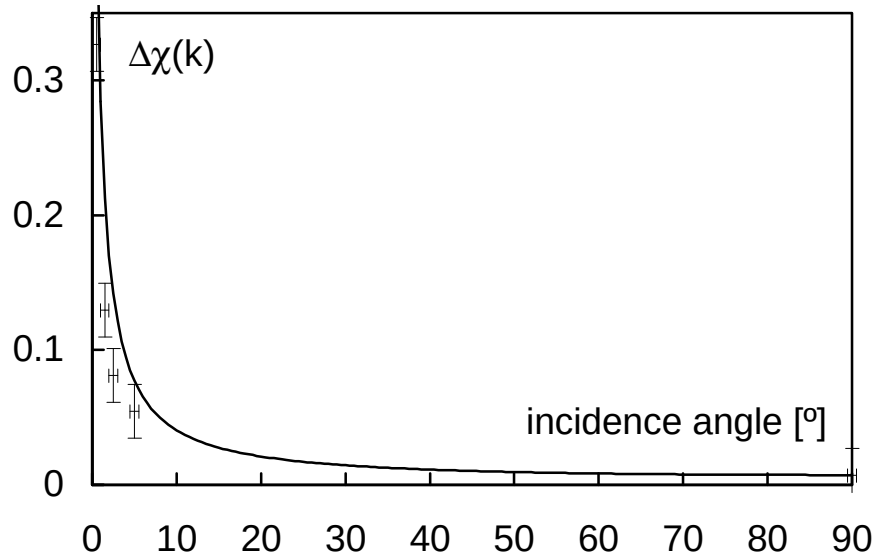

Figure 4.2.7. Experimental data for pressed pellet of ZnO compared to the predictions of eq. (4.2.8). Calculation parameters: l = 727 Å, $\overline{m}_{tot}(E)$ = 181.3 cm^2/g, $\overline{m}(E)$ = 287.4 cm^2/g, density = 5.61 g/cm^3.

It is immediately obvious from inspection of figures 4.2.5 - 4.2.7 that the calculations of $Dc(k)$ overestimate the experimental amplitude reductions significantly. The deviations are smallest for Cr, and largest for Ni. The reason for the discrepancies becomes clear when the influence of the fluorescence-yield on the TEY signal is considered. Fluorescent photons from the sample excite photoelectrons with kinetic energies comparable to the KLL Auger electron energies. The fluorescence-derived TEY contribution therefore undergoes similar gas-phase amplification as the Auger channel and the well-known 'self-absorption' effect in the fluorescence-yield becomes visible in the TEY signal. A quantitative model which predicts the magnitude of this effect will be derived in detail in section 4.3. Here it shall suffice to point out that the TEY signal excited by the incident X-rays is much more sensitive to changes in the X-ray incidence angle J than the fluorescence-derived TEY fraction. The TEY increases strongly towards low incidence angles because the fraction of incoming X-rays absorbed in the near-surface region of the sample increases. In comparison, the TEY contribution excited by the fluorescence-yield signal responds much less to the reduced X-ray penetration of the sample because the attenuation of the fluorescent photons is intrinsically small. Because the sample is much more 'transparent' to the photons, small changes in their depth distribution function due to angular variation are only weakly reflected by the intensity of the emitted flux. This can also be understood by inspection of eqs. (4.2.6) and (4.2.5b): the influence of $\sin J$ in eq. (4.2.6) is much weaker than in eq. (4.2.5b) because the

absorption coefficient $m_{tot}(E_f)$ is much smaller than $1/l(E_p)$. The result of an exact calculation of the fluorescence-yield effect on the amplitude reduction in the TEY of Ni is given in figure 4.2.8.

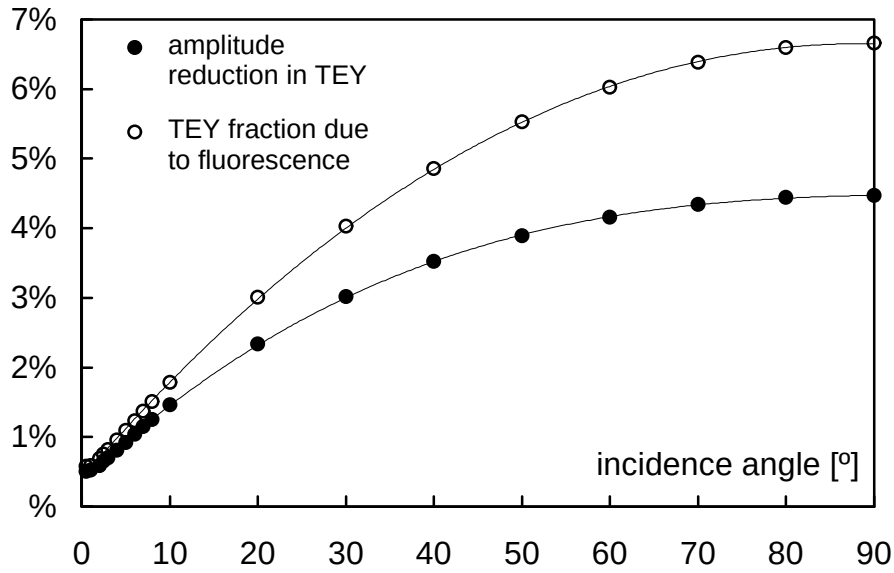

Figure 4.2.8. Incident angle dependence of the fluorescence-derived TEY contribution from Ni metal (open circles) and the corresponding fluorescence-yield derived EXAFS amplitude reduction (filled circles). Because the fluorescence-yield induced 'self-absorption' correction is a strong function of the fluorescence-yield contribution to the TEY it becomes small at low incidence angles. The calculations were carried out using eqs. 4.3.6 and 4.3.10.

Figures 4.2.9 - 4.2.11 compare the experimental data to the predictions of eqs. (4.2.7) and (4.2.8) after the correction for the angular variation of the fluorescence-yield related 'self-absorption' effect has been introduced. Agreement between experiment and theory is now excellent for all data. Note that the correction for Cr is comparatively small due to the relatively low probability for fluorescence decay (0.275) of Cr K core vacancies. The probabilities for radiative decay of K-holes in Ni (0.406) and Zn (0.474) are higher, resulting in a larger effect of the fluorescence.

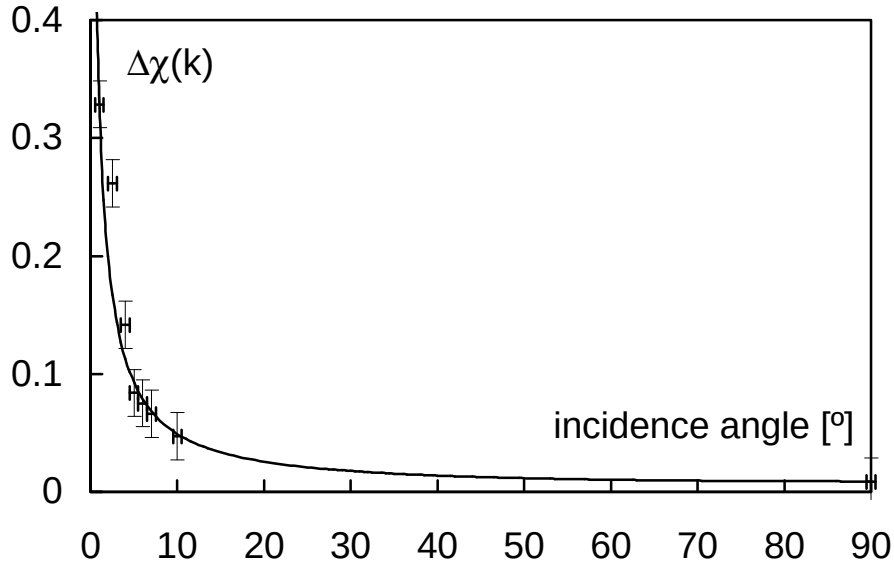

Figure 4.2.9. Experimental data for the polished Ni wafer corrected for the contribution of self-absorbed fluorescence. Calculation parameters are given in the caption of figure 4.2.6.

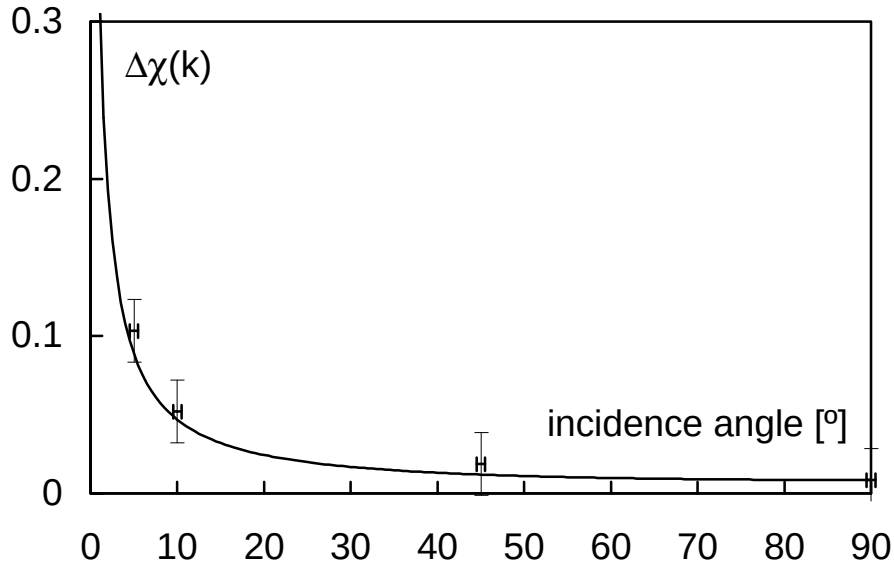

Figure 4.2.10. Experimental data for the Cr(110) single crystal corrected for the contribution of self-absorbed fluorescence. Calculation parameters are given in the caption of figure 4.2.5.

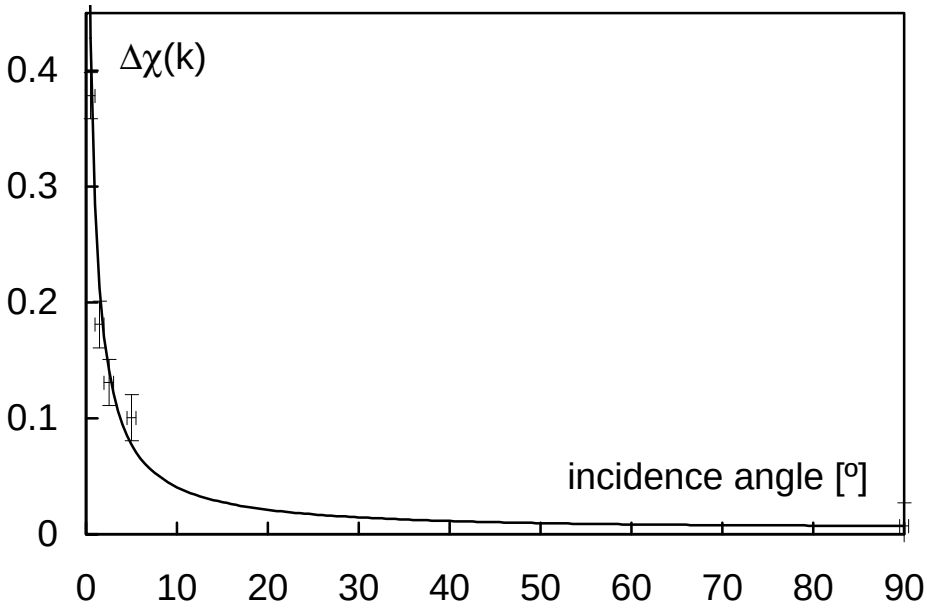

Figure 4.2.11. Experimental data for the ZnO pellet corrected for the contribution of self-absorbed fluorescence. Calculation parameters are given in the caption of figure 4.2.7.

4.3. Fluorescence-Induced 'Self-Absorption' Effect in TEY XAS

4.3.1. Introduction

Implicitly assuming that the electron escape region is identical to the sample volume probed by TEY detection, it has repeatedly been suggested in the literature that the technique is *entirely free* from any 'self-absorption' and 'thickness' effects [29,41-44]. In the preceding sections of this chapter it has already been shown that a 'self-absorption' correction does apply to TEY data measured at grazing X-ray incidence angles. This analysis did not challenge the above assumption that the escape volume of the TEY is identical to the sample region probed by the signal. Calculations and experimental data presented in the following sections will now prove that this view is indeed oversimplifying the TEY signal formation process. The TEY from optically dense samples with a sufficiently high fluorescence-yield (FY) contain photoelectrons excited by fluorescent photons carrying bulk information. As a result, the TEY signal exhibits the well-known amplitude distortions inherent in the FY channel - albeit to a smaller extent.

4.3.2. Model Calculation

For a semi-infinite sample with a flat surface in the (x,y)-plane of a right-handed Cartesian coordinate system, the magnitude of the amplitude reduction Δc_{tot}^{TEY} can be predicted as follows. Assuming that the angular distribution of fluorescence emission from each atom is isotropic in angle and that the irradiated area of the sample surface is small compared to the total surface area, the emitted flux of photons from depth z in the sample into the direction defined by the spherical coordinates q (polar angle) and f (azimuthal angle) is given by

$$dI_f(E,J,q,f,z) = I_0(E,J,z)\cdot P(E_f,q,z)\cdot w\cdot m(E)\cdot\frac{\sin q}{4p}\cdot dq\cdot df\cdot dz, \quad (4.3.1)$$

where J is the angle of X-ray incidence with respect to the sample surface, E the energy of the incident X-ray photons, ω the probability for radiative decay of each X-ray induced primary core hole [62], and $m(E)$ the linear absorption coefficient for photoemission from the atomic orbital responsible for the absorption edge of interest [27]. The intensity $I_0(E,J,z)$ of the incident X-ray beam depends on the depth z in the sample according to

$$I_0(E,J,z) = I_0(E)\cdot\exp\left(-m_{tot}(E)\cdot z/\sin J\right), \quad (4.3.2)$$

where $m_{tot}(E)$ is the total linear absorption coefficient at photon energy E [27] and $I_0(E)$ the X-ray intensity at the sample surface. Every fluorescent photon of energy E_f travelling towards the surface of the sample has an escape probability $P(E_f,z,q)$, as determined by the total linear absorption coefficient $m_{tot}(E_f)$ at the energy E_f [27]:

$$P(E_f,q,z) = \exp\left(-m_{tot}(E_f)\cdot z/\sin q\right), \quad (4.3.3)$$

For an infinitely thick sample, integration of eq. (1) over all z and all azimuthal angles yields the total FY intensity $I_f(E,J,q)$ emitted in the direction defined by q as

$$I_f(E,J,q) = \frac{1}{2}\cdot I_0(E)\cdot w\cdot m(E)\cdot\frac{\sin^2 q}{m_{tot}(E)\cdot\sin q + m_{tot}(E_f)\cdot\sin J}. \quad (4.3.4)$$

Only a small fraction of the fluorescence is absorbed in the near-surface region of thickness d from which the TEY signal derives because d is typically two orders of magnitude shorter than the sample penetration by the fluorescence [4,63]. The actual flux of fluorescent photons through the near-surface layer can therefore be approximated by the emitted flux $I_f(E,J,q)$. The probability $P_f^{TEY}(E_f,q)$ that a fluorescent photon of energy E_f is absorbed in a layer of thickness d is given by

$$P_f^{TEY}(E_f,q) = 1-\exp(-m_{tot}(E_f)\cdot d/\sin q), \quad (4.3.5)$$

and the TEY contribution excited by fluorescent photons thus by

$$I_f^{TEY}(E,J) \approx A(E)\cdot \int_0^{p/2} I_f(E,J,q)\cdot P_f^{TEY}(E_f,q)\cdot dq, \quad (4.3.6)$$

where $A(E)$ is an amplification function which takes account of charge multiplication due to secondary electron production and/or core vacancy multiplication (cf. chapter 3 and refs. [4,7]).

The energy of the photoelectrons excited by fluorescence is, within an error negligible in the present context, equal to the energy of the Auger electrons emitted in the first step of the radiationless core hole decay. This fact simplifies the calculation of the FY-excited contribution to the TEY considerably. Firstly, Auger electrons produced by the incident X-rays and photoelectrons excited by the fluorescence escape from the sample with identical depth distribution functions. Secondly, the amplification function $A(E)$ applies equally to both TEY contributions. The absorption edge signal $I_0^{TEY}(E,J)$ excited by the incident X-ray beam is thus given by

$$I_0^{TEY}(E,J) \approx I_0(E)\cdot A(E)\cdot a_0\cdot m(E)\cdot \int_0^{d} \exp(-m(E)\cdot z/\sin J)\cdot dz, \quad (4.3.7)$$

where a_0 denotes the probability for radiationless decay of the core hole formed by absorption of an incident X-ray [62]. It should be mentioned that eq. (4.3.7) neglects the additional TEY contribution due to the radiationless decay of secondary vacancies which are formed in higher atomic shells during the neutralisation of the

X-ray induced primary core hole [4,7]. However, this contribution is usually small (typically 10% of the vacuum TEY current, *vide supra* and ref. [4]) and can be neglected. This is especially true for gas-flow TEY detection where charge amplification in the gas phase weights the signal towards the more energetic Auger electron contributions emitted in the first step of the radiationless core hole decay [7].

The EXAFS amplitude reduction $\Delta c(E,q)$ associated with each fluorescence emission angle q is, for a semi-infinite sample, given by the smooth, 'atomic' contributions $\overline{m}(E)$ to the absorption coefficient [27] according to [18,19,21]

$$\Delta c(E,J,q) \approx \frac{\overline{m}(E)}{\overline{m}_{tot}(E) + \overline{m}_{tot}(E_f) \cdot \sin J \,/\, \sin q}. \qquad (4.3.8)$$

The amplitude reduction $\Delta\overline{c}(E,J)$ carried by the fluorescence-derived TEY contribution is then given by

$$\Delta\overline{c}(E,J) \approx 1/\, I_f^{TEY}(E,J) \cdot \int_0^{p/2} \Delta c(E,J,q) \cdot I_f(E,J,q) \cdot P_f^{TEY}(E_f,J) \cdot dq\,, \qquad (4.3.9)$$

and the amplitude reduction $\Delta c_{\,TEY}(E,J)$ in the measured TEY signal by

$$\Delta c_{\,TEY}(E,J) \approx \frac{\Delta\overline{c}(E,J) \cdot I_f^{TEY}(E_f,J)}{I_f^{TEY}(E_f,J) + I_0^{TEY}(E,J)}. \qquad (4.3.10)$$

Note that knowledge of the parameter $A(E)$ is not necessary, as it cancels out in the calculation. The calculation is also very insensitive to the exact value of d. The present results were obtained using the rule derived in section 3.10. which states that the depth of the Auger electron escape region equals approximately half the total Auger electron range (Bethe range, R_B). A program for the automated evaluation of eq. (4.3.10) for any given material has been written for the Microsoft Windows® operating system (copies can be obtained from the author). It is based on a numerical quadrature method (Romberg integration [68,69]) for the integrations over q.

4.3.3. Experimental

To test the predictions derived from eqs. (1) - (10), TEY data from several polycrystalline transition metal samples (temper-annealed foils of Ni, Pd, Pt and Au, 99.9% pure) were compared to reference transmission spectra. One set of foils was optically dense, thus to attenuating the X-ray beam in the post-edge region of the spectrum by more than 99.9% (table 4.3.1). All these foils were mounted on a ceramic support block which eliminated spurious fluorescence- and electron-yield contributions from the rear surface of the sample. Two Ni wafers were diamond-polished to a final grain size of 0.5 μm and annealed at 600°C in a flow of H_2 to remove the damage layer introduced by the polishing process. One of these wafers was coated with a 400 Å (± 25%) film of Au. All samples were stored in ambient air prior to data collection on beamlines 8.1 (Ni) and 9.2 (Au, Pt, Pd) of the EPSRC synchrotron facility in Daresbury/U.K. The storage ring was operating at 2 GeV energy and with electron currents between 140 mA and 240 mA. Rejection of higher beam harmonics was performed by detuning the double-crystal Si(220) monochromators to 50% of maximum reflectivity. A system of slits ensured that the X-ray illuminated area of the sample surfaces was small compared to the total sample surface area. The incident X-ray flux was monitored by ion chambers (20% absorbance at the edge) containing mixtures of He and Ar. The gas-flow TEY detector used for the measurements was the cell described in section 2.6. The experimentally employed angles of X-ray incidence with respect to the sample surface are given in table 4.3.1. Grazing incidence angles were not employed because of the additional 'self-absorption' distortions of the XAFS under these conditions (cf., section 4.2). Comparative transmission data for a set of thin (Pt: 4 μm, Au: 5 μm, Pd, Ni: 8 μm) metal foils were obtained at normal X-ray incidence employing a second ion chamber (absorbance: 80%) as the monitor for the transmitted beam. Additional FY-spectra of several samples were obtained with a 13-element solid-state detector positioned at an angle of 45° with respect to the sample surface.

4.3.4. Results and Discussion

After normalisation to the edge step height, the presence of any 'self-absorption' effects can be verified by inspection of the near-edge region of the spectrum [9,19,23]. Particularly diagnostic are pre-edge features and the slope of the edge step, both of which appear artificially enhanced relative to the post-edge oscillations when a 'self-absorption' distortion is present. This effect is clearly visible in figure 4.3.1. which compares pre-edge subtracted, normalised near-edge FY- and TEY-data from an optically dense Pd foil to a standard transmission spectrum of Pd. Both the FY-

and the TEY-spectrum exhibit characteristic 'self-absorption' deviations from the reference spectrum, but the distortions in the TEY spectrum are considerably weaker. 'Self-absorption' distortion are also illustrated in figure 4.3.2. which plots K-edge TEY data from Ni wafers with and without a 400 Å Au-overlayer against a reference transmission spectrum of Ni. The TEY spectrum of the Au-covered wafer exhibits a substantial 'self-absorption' effect, while deviations between the TEY spectrum of the uncoated sample and the reference are almost negligible. The striking difference between the TEY spectra of Ni derives undoubtedly from the Au overlayer which attenuates the TEY contributions from the radiationless decay of K-vacancies in the underlying Ni substrate. The experimental Ni K-edge step height in the TEY spectrum of the Au-coated sample was indeed only 13% (± 2%) of the value for the clean Ni wafer. Because the radiationless channel is strongly attenuated, the FY-derived photoelectron signal becomes a substantial fraction of the TEY from the coated wafer. As a result, the 'self-absorption' effect in the FY channel appears pronounced in the TEY signal. Note that other effects are also expected to influence the actual magnitude of the FY-derived contribution to the TEY. Most importantly, the presence of the Au overlayer enhances the photoelectron flux because the coefficient for absorption of the Ni K-fluorescence by Au is an order of magnitude higher than the corresponding value in Ni [27]. Note also that this enhancement could be offset by the larger electron stopping power of Au or the lower energy of the photoelectrons emitted from the Au overlayer. In fact, the latter dominates as the Au M-shell (from which most photoelectrons from the coated wafer originate) is more tightly bound than the Ni L-shell (which contributes most photoelectrons from the uncoated wafer). A systematic study of the interplay between the several amplification and attenuation mechanisms in overlayers is the subject of ongoing investigations by the author. It appears unquestionable, however, that the predominant effect of the Au overlayer is the enhancement of the FY-derived TEY fraction *via* suppression of contributions from the radiationless decay channel.

Table 4.3.1. Results of the data analysis for the fluorescence-yield induced 'self-absorption' effect compared to calculated predictions.

	thickness	w	J	$\mu_{tot}(E_0)$	$\mu_{tot}(E_f)$	$\mu(E_0)$	$\Delta c_{tot}(E_0,q,J)$, q = 45°		$\Delta c_{tot}^{TEY}(E_0,J)$	
	[μm]				[μm^{-1}]		calc.	experim.	calc.	experim.
Ni	1000	0.406	90°	0.294	0.053	0.258	0.70	n/a	0.045	0.09 ± .03
Ni	1000 (+Au)	0.406	60°		n/a		n/a	n/a	n/a	0.35 ± .03
Pd	8	0.820	60°	0.070	0.016	0.059	n/a	0.25 ± .03	n/a	0.13 ± .03
Pd	125	0.820	60°	0.070	0.016	0.059	0.64	0.66 ± .03	0.222	0.26 ± .03
Pt	100	0.306	60°	0.397	0.272	0.236	0.30	0.33 ± .03	0.028	0.03 ± .03

Au	250	0.320	60°	0.352	0.193	0.209	0.30	n/a	0.030	0.03 ± .03

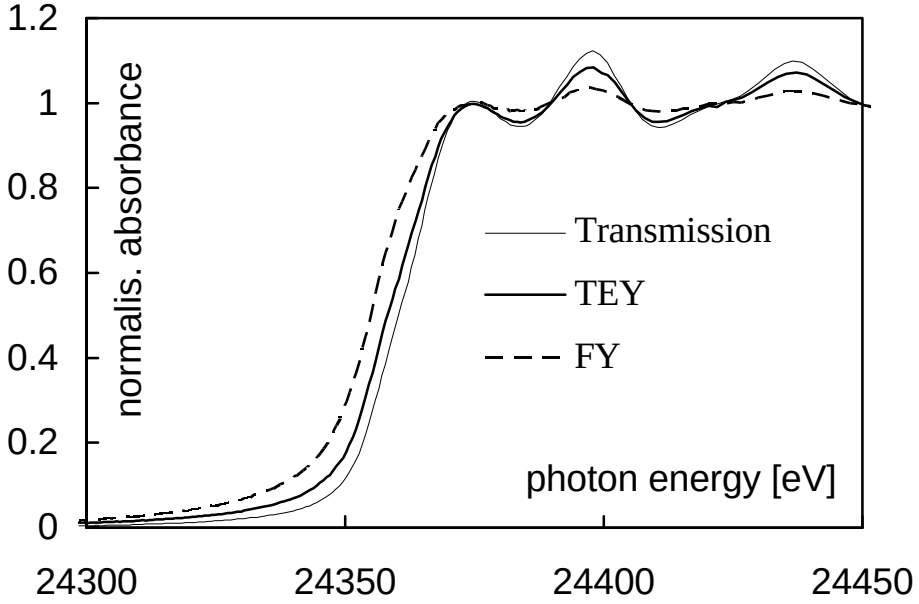

Fig. 4.3.1. Near-edge spectra of the 125 μm Pd foil measured *via* its FY and TEY compared to the near-edge transmission spectrum of a 8 μm Pd foil.

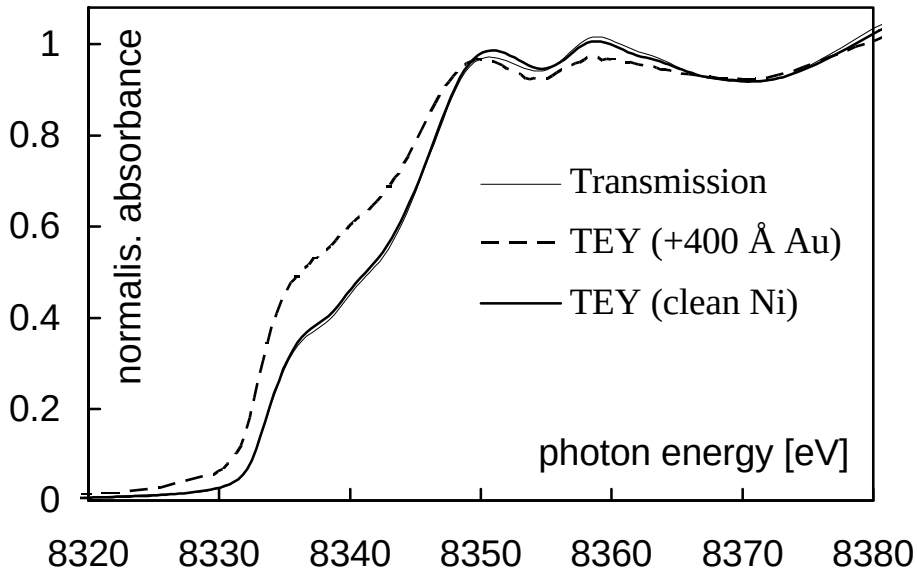

Fig. 4.3.2. TEY near-edge spectra of a 1 mm thick, polished Ni wafer with a clean surface (full, thick line) and covered by 400 Å of Au (thick, broken line) compared to the near-edge transmission spectrum (thin full line) of a 8 μm Ni foil.

The corresponding EXAFS functions are presented in figure 4.3.3. Amplitude reductions are clearly visible in several of the spectra. The magnitude of the reductions was quantified by the scaling factors which afforded best least-squares

agreement with the corresponding reference spectrum. No k-weighting was employed for this analysis. In table 4.3.1, results are compared to calculated values. The experimental values for $\Delta c_{TEY}(E,J)$ are, within the error margins, in quite good agreement with the predictions of eqs. (1)-(10). That the amplitude reductions are indeed due to a self-absorbed fraction of the FY is underlined by the fact that the TEY spectrum of the 8 μm Pd foil (used also as the transmission standard) exhibited a clear amplitude reduction, but to a smaller degree than the optically dense 125 μm foil (table 4.3.1). This result is expected because, although the 8 μm sample is optically considerably less dense than the 125 μm foil, it is still too dense for a meaningful XAFS amplitude determination. The small amplitude reductions which were predicted and observed for the TEY L_3-edge spectra of Pt and Au as well as for the K-edge spectrum of Ni are in good agreement with previous experimental TEY results for these materials [28,29].

Some uncertainty in the experimental figures for $\Delta c_{TEY}(E,J)$ is due to oxide formation and/or disorder near the sample surface. Furthermore, a fraction of the FY is expected to irradiate the biased collector plate in the detector and to excite additional photoelectrons, adding an extra 'self-absorption' component to the measured TEY signal. The magnitude of this effect can be estimated from the acceptance angle subtended by the detector plate over the sample. During the present experiments it was approximately $\pi/2$ steradians, suggesting that the calculations could be underestimating the true amplitude reduction by as much as 25%. Indeed, the experimental value of $\Delta c_{TEY}(E,J)$ for Pd is somewhat larger than the calculated figure (table 4.3.1). Similar deviations are not seen for the other samples investigated here because the additional amplitude modifications are well below the error margin of the measurement.

4.4. Summary and Suggestions for Future Work

Unequivocal evidence for a 'self-absorption' distortion intrinsic to TEY detection has been presented. The magnitude of this effect can be accounted for by TEY contributions excited by fluorescent photons. The effect is particularly strong for optically dense samples with a high FY, such as at the Pd K-edge, and in experimental situations where the FY contribution is artificially amplified, as in the presented case of a Au-coated Ni sample. Similar amplification effects might contribute to the amplitude reductions observed in the TEY spectra of thin films [5]. Most materials, especially compounds, are sufficiently optically dilute to render any 'self-absorption' effect in the TEY signal negligible. Current work is considering the

-absorption' distortion on film thickness and the presence of

support materials. XAFS measurements on Pd and Pt following the dependence on film thickness (the raw Pd data are presented in fig. 4.3.4) have already been carried out by the author. The spectra provide additional evidence that the normal-incidence self-absorption effect in the TEY-data is due to excitations by fluorescent photons: for very thin foils, the EXAFS amplitudes of TEY- and FY-data are identical. Amplitude reductions in the TEY channel only occur when the foil thickness becomes large enough to permit a significant 'self-absorption' distortion in the FY-channel. A detailed analysis of these data is complicated, as the simple analytical theory for semi-infinite samples presented above is not applicable in this case. Future work will also address the influence of surface roughness and sample morphology (small particles, powders) on the TEY amplitude.

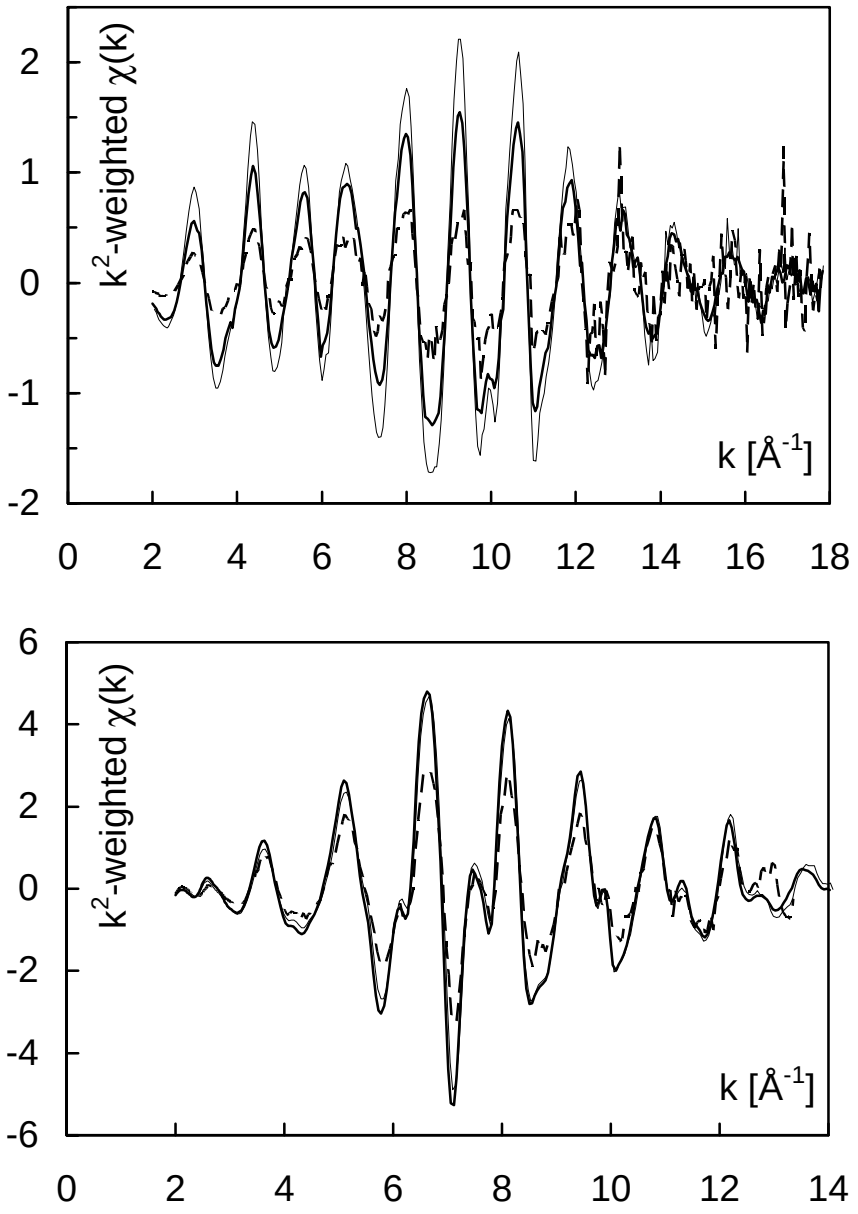

Fig. 4.3.3. k^2-weighted EXAFS functions corresponding to the near-edge data in figs. 4.3.1 and 4.3.2. Upper diagram: Pd metal K-edge spectra. Thin, full line, 8 μm foil in transmission mode; thick full line: 125 μm foil in TEY mode; broken line: 125 μm foil in FY mode. Lower diagram: Ni metal K-edge spectra. Thin, full line, 8 μm foil in transmission mode; thick full line: 1 mm wafer in TEY mode; broken line: 1 mm wafer covered by 400 Å of Au in TEY mode.

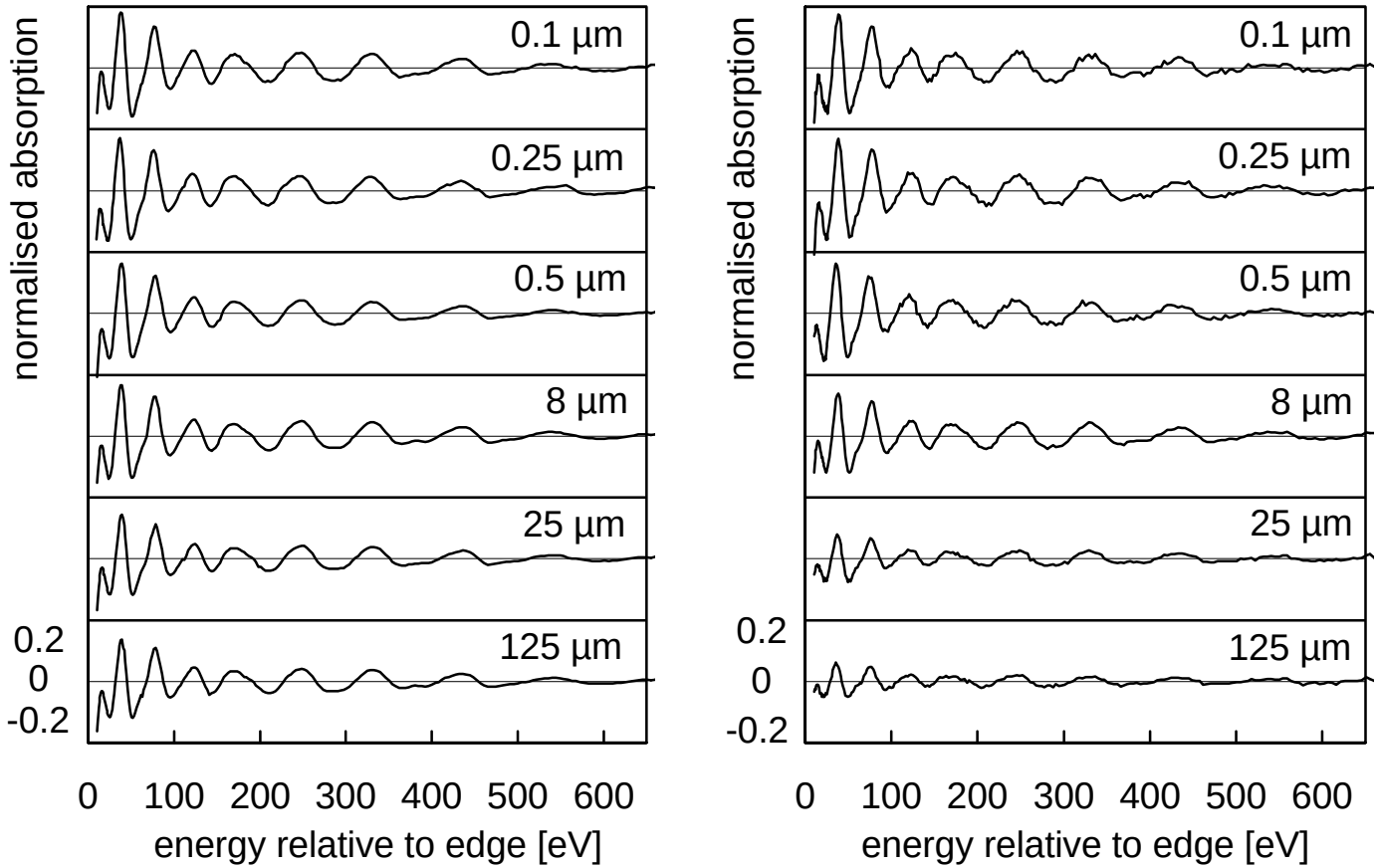

Fig. 4.3.4. Unweighted Pd K-edge EXAFS spectra as a function of sample thickness. Left column: TEY-data. Right column: FY-data. The sample thicknesses are given as insets to the spectra.

4.5. References

[1] A.M. Edwards, Y. Dao, R.J. Nemanich, D.E. Sayers, K.M. Kemner, J. Appl. Phys. 76 (1994) 4630.

[2] T.K. Sham, R.G. Carr, J. Chem. Phys. 83 (1985) 5914.

[3] P. Crespo, A. Hernando, A.G. Escorial, K.M. Kemner, V.G. Harris, J. Appl. Phys. 76 (1994) 6322.

[4] A. Erbil, C.S. Cargill III, R. Frahm, R.F. Boehme, Phys. Rev. B 37 (1988) 2450.

[5] Y.U. Idzerda, W.T. Elam, B.T. Jonker, G.A. Prinz, Phys. Rev. Lett. 62 (1989) 2480.

[6] T. Guo, M.L. denBoer, Phys. Rev. B 31 (1985) 6233.

[7] S.L.M. Schroeder, G.D. Moggridge, R.M. Ormerod, T. Rayment, R.M. Lambert, Surf. Sci. Lett. 324 (1995) L371.

[8] Y.U. Idzerda, B.T. Jonker, W.T. Elam, G.A. Prinz, J. Appl. Phys. 67 (1990) 5385.

[9] G.G. Long, D.A. Fischer, J. Kruger, D.R. Black, D.K. Tanaka, G.A. Danko, Phys. Rev. B 39 (1989) 10651.

[10] E.D. Crozier, J.J. Rehr, R. Ingalls, *Amorphous and Liquid Systems,* in: X-ray Absorption: Principles, Applications, Techniques of EXAFS, SEXAFS and XANES, ed. by D.C. Koningsberger and R. Prins (Wiley-Interscience, New York, 1988) 373.

[11] M.J. van der Hoek, W. Werner, P. van Zuylen, B.R. Dobson, S.S. Hasnain, J.S. Worgan, G. Luijckx, Nucl. Instrum. Methods A 246 (1986) 380.

[12] M. Oversluizen, G.E. Derbyshire, C. Morrell, R. Farrow, B.R. Dobson, Rev. Sci. Instrum. 63 (1992) 924.

[13] *Gmelins Handbuch der Anorganischen Chemie. System-Nummer 57. Nickel. Teil B - Lieferung 2* (Verlag Chemie, Weinheim, 1966).

[14] C.R. Brundle, J.Q. Broughton, *The initial interaction of oxygen with well-defined transition metal surfaces,* in: The Chemical Physics of Solid Surfaces and Heterogeneous Catalysis Vol.3: Chemisorption Systems, Part A, ed. by D.A. King and D.P. Woodruff (Elsevier, Amsterdam, Oxford, New York, Tokyo, 1990) 131.

[15] R.G. Musket, W. McLean, C.A. Colmenares, D.M. Makowiecki, W.J. Siekhaus, Appl. Surf. Sci. 10 (1982) 143.

[16] E.A. Stern, *Theory of EXAFS,* in: X-Ray Absorption. Principles, Applications, Techniques of EXAFS, SEXAFS and XANES, ed. by D.C. Koningsberger and R. Prins (John Wiley & Sons, New York, Chichester, Brisbane, Toronto, Singapore, 1988) 351.

[17] R.W. Joyner, K.J. Martin, P. Meehan, J. Phys. C 20 (1987) 4005.

[18] J. Goulon, C. Goulon-Ginet, R. Cortes, J.M. Dubois, J. Phys. (Paris) 43 (1982) 539.

[19] Z. Tan, J.I. Budnick, S.M. Heald, Rev. Sci. Instrum. 60 (1989) 1021.

[20] L. Tröger, E. Zschech, D. Arvanitis, K. Baberschke, Jpn. J. Appl. Phys 32-2 (1993) 144.

[21] L. Tröger, D. Arvanitis, K. Baberschke, H. Michaelis, U. Grimm, E. Zschech, Phys. Rev. B 46 (1992) 3283.

[22] E. Zschech, L. Tröger, D. Arvanitis, H. Michaelis, U. Grimm, K. Baberschke, Solid State Commun. 82 (1992) 1.

[23] D.M. Pease, D.L. Brewe, Z. Tan, J.I. Budnick, C.C. Law, Phys. Letters A 138 (1989) 230.

[24] T.M. Hayes, J.B. Boyce, Solid State Phys. 37 (1982) 173.

[25] D.T. Jiang, E.D. Crozier, Nucl. Instrum. Methods A 294 (1990) 666.

[26] D.T. Jiang, E.D. Crozier, B. Heinrich, Phys. Rev. B 44 (1991) 6401.

[27] B.L. Henke, E.M. Gullikson, J.C. Davis, At. Data Nucl. Data Tables 54 (1993) 181.

[28] K.I. Pandya, K. Yang, R.W. Hoffman, W.E. O'Grady, D.E. Sayers, J. Phys. (Paris) Colloque C8 (1986) 159.

[29] K.M. Kemner, Z. Wang, R.A. Mayanovic, B.A. Bunker, Nucl. Instrum. Methods B 71 (1992) 345.

[30] L.V. Azároff, B.N. Das, Phys. Rev. 134 (1964) A747.

[31] L.G. Parratt, C.F. Hempstead, E.L. Jossen, Phys. Rev. 105 (1957) 1228.

[32] S.M. Heald, *Design of an EXAFS Experiment,* in: X-Ray Absorption: Principles, Applications, Techniques of EXAFS, SEXAFS and XANES, ed. by D.C. Koningsberger and R. Prins (John Wiley & Sons, New York, Chichester, Brisbane, Toronto, Singapore, 1988) 87.

[33] E.A. Stern, K. Kim, Phys. Rev. B 23 (1981) 3781.

[34] K.-Q. Lu, E.A. Stern, Nucl. Instrum. Methods 212 (1983) 475.

[35] J. Jaklevic, J.A. Kirby, M.P. Klein, A.S. Robertson, G.S. Brown, P. Eisenberger, Solid State Commun. 23 (1977) 679.

[36] R.F. Boehme, C.S. Cargill III, W. Weber, T. Jackson, J. Appl. Phys. 58 (1985) 811.

[37] W. Gudat, C. Kunz, Phys. Rev. Lett. 29 (1972) 169.

[38] G. Martens, P. Rabe, N. Schwentner, A. Werner, J. Phys. C 11 (1978) 3125.

[39] G. Martens, P. Rabe, G. Tolkiehn, A. Werner, Phys. Stat. Sol. A 55 (1979) 105.

[40] R.G. Jones, D.P. Woodruff, Surf. Sci. 114 (1982) 38.

[41] G. Meitzner, J.H. Sinfelt, Catal. Lett. 30 (1995) 1.

[42] E.A. Stern, R.W. Siegel, M. Newville, P.G. Sanders, D. Haskel, Phys. Rev. Lett. 75 (1995) 3874.

[43] J.A. Eastman, M.R. Fitzsimmons, M. Müller-Stach, G. Wallner, W.T. Elam, Nanostruct. Mater. 1 (1992) 47.

[44] I.H. Song, B. Rickett, P. Janavicius, J.H. Payer, M.R. Antonio, Nucl. Instrum. Methods A 360 (1995) 634.

[45] A. Stierle, P. Bödeker, H. Zabel, Surf. Sci. 327 (1995) 9.

[46] G. Thurner, P.H. Holloway, Acta Physica Polonica A 81 (1992) 273.

[47] N.M.D. Brown, H.-X. You, Surf. Sci. 233 (1990) 317.

[48] C. Palacio, H.J. Mathieu, D. Landolt, Surf. Sci. 182 (1987) 41.

[49] J.C. Peruchetti, C. Pirri, D. Bolmont, G. Gewinner, Solid State Commun. 59 (1986) 517.

[50] J.S. Foord, R.M. Lambert, Surf. Sci. 161 (1985) 513.

[51] G. Gewinner, J.C. Peruchetti, A. Jaéglé, Surf. Sci. 122 (1982) 383.

[52] Y. Sakisaka, H. Kato, M. Onchi, Surf. Sci. 120 (1982) 150.

[53] F. Watari, J.M. Cowley, Surf. Sci. 105 (1981) 240.

[54] G.C. Allen, P.M. Tucker, R.K. Wild, J. Chem. Soc. Faraday Trans. II 74 (1978) 1126.

[55] G. Gewinner, J.C. Peruchetti, A. Jaéglé, A. Kalt, Surf. Sci. 78 (1978) 439.

[56] C. Jardin, P. Michel, Surf. Sci. 71 (1978) 575.

[57] S. Ekelund, C. Leygraf, Surf. Sci. 40 (1973) 179.

[58] P. Michel, C. Jardin, Surf. Sci. 36 (1973) 478.

[59] H.M. Kennett, A.E. Lee, Surf. Sci. 33 (1972) 377.

[60] J.J. Yeh, I. Lindau, At. Data Nucl. Data Tables 32 (1985) 1.

[61] B.L. Henke, E.M. Gullikson, J.C. Davis, At. Data Nucl. Data Tables 55 (1993) 349.

[62] M.O. Krause, J. Phys. Chem. Ref. Data 8 (1979) 307.

[63] S.L.M. Schroeder, Solid State Commun. 98 (1996) 405.

[64] S.I. Salem, S.L. Panossian, S.O. Krause, At. Data Nucl. Data Tables 14 (1974) 91.

[65] J. Jaklevic, J.A. Kirby, M.P. Klein, A.S. Robertson, G.S. Brown, P. Eisenberger, Solid State Commun. 88 (1993) 1105.

[66] L. Tröger, D. Arvanitis, H. Rabus, L. Wenzel, K. Baberschke, Phys. Rev. B 41 (1990) 7297.

[67] J. Goulon, J. Chim. Phys. 86 (1989) 1427.

[68] W.H. Press, B.P. Flannery, S.A. Teukolsky, W.T. Vetterling, *Numerical Recipes in Pascal. The Art of Scientific Computing* (Cambridge University Press, Cambridge, U.K. 1989).

[69] J.C. Sprott, *Numerical Recipes. Routines and Examples in Basic* (Cambridge University Press, Cambridge,U.K. 1991).